In silico high throughput screening of Manganese-based complexes for binding of pyridine in catalytic homogeneous hydrogenation

Azaima Khan

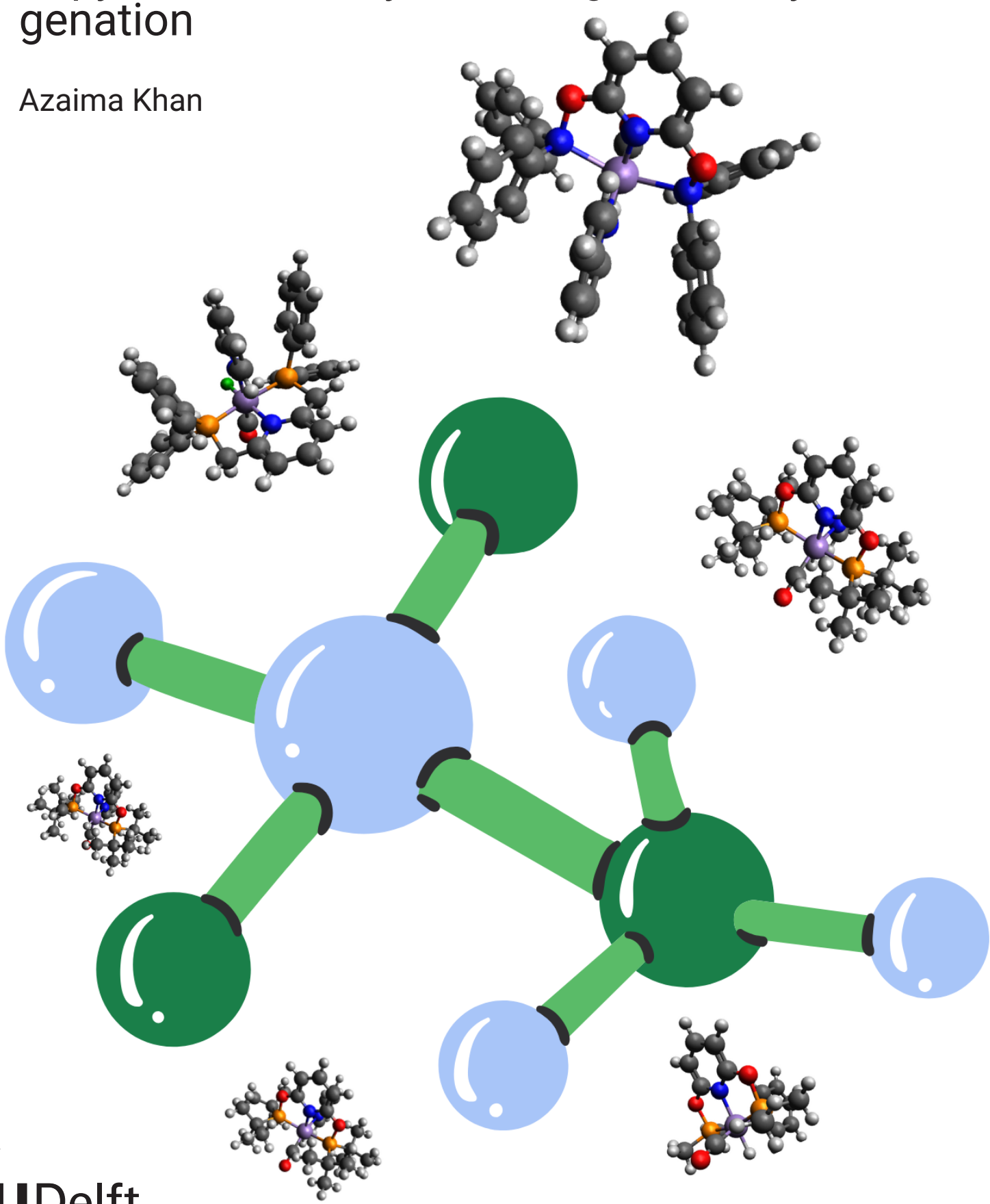

Delft University of Technology

TU Delft

In silico high throughput screening of Manganese-based complexes for binding of pyridine in catalytic homogeneous hydrogenation

by

Azaima Khan

to obtain the degree of Bachelor of Science

at the Delft University of Technology,

to be defended publicly on Tuesday July 22, 2025 at 13:00 PM.

Performed at:
Inorganic Systems Engineering
Chemical Engineering
Faculty of Applied Sciences

Under supervision of:
Prof. Dr. E. A. Pidko
PhD(c). A. Kalikadien
Dr. A. A. Kolganov

Student number: 5472938/s3675483
Project duration: April 22, 2025 – July 22, 2025
Thesis committee: Prof. Dr. E. A. Pidko, TU Delft, supervisor
Prof. Dr. T. Bouwens, TU Delft

TU Delft

ISEgroup
ChemE @ TU Delft

Abstract

Addressing the resources needed to produce sustainable and environmentally friendly products is key within the field of catalysis. One of the key applications of catalysis is the storage of renewable hydrogen. This could be achieved through liquid organic hydrogen carriers (LOHCs), which participate in homogeneous catalysis. This field emphasizes high selectivity through the use of transition-metal complexes. A suitable LOHC candidate could be pyridine, a type of N-heterocycle, which serves as a benchmark for successful binding to the metal complex. The binding of pyridine can be enhanced by substituting noble metals with transition metals, such as manganese, which has shown promising catalytic activity. We perform high-throughput screening with DFT calculation for the following systems: PNP, PONOP, NNN, and NONON, which vary in their backbones. Every metal complex consists of three various configurations: the alignment of the auxiliary carbonyl ligand with the hydride atom (config 1), pyridine (config 2) and the lutidine part of the nitrogen pincer atom (config 3). The catalytic performance is studied by determining the stable and reactive complexes, as well as their specific configurations. Only positive binding energies, in terms of the $\Delta G_{\text{reaction}}$, are observed. This indicates that no complexes show strong binding of the metal to pyridine. However, the phenyl-substituted system exhibits the lowest binding energies, of which the third configuration is the most favored for all ligand types. This holds for the trans-positioning of the auxiliary carbonyl ligand with the lutidine part of the nitrogen pincer atom, mainly for the NNN-based complex. Still, the preferred configurations do not correlate with the strengthened metal-pyridine binding and weakening of the metal-auxiliary carbonyl ligand bond length. In terms of reactivity, the nitrogen-based complexes show the highest hydride charges, which could be assumed to provide high reactivity. However, the hydridic behavior of the complexes does not correspond with the stability of the phenyl substituents and all remaining complexes. After the reactivity of the complexes is considered, we can enable fine-tuning of specific backbones to forecast trends observed in reactivity. The phenyl-substituent can be used as a starting point due to its delocalized system and electron-donating property for fine-tuning. Nitrogen-based complexes enable fine-tuning of the reactivity because they depend on the ligand scaffold rather than the substituents. In addition, variation in binding energies for every substituent is most commonly observed for nitrogen-based complexes. The nitrogen-based complex can therefore be used to perform improved ligand design with the fine-tuning ability of the phenyl substituent.

Contents

List of Figures

1 Introduction

1.1. Homogeneous hydrogenation catalysis

The generation of resources to meet human needs is primarily a matter of catalysis. Within the chemical industry, it is crucial to select the right characteristics to create an effective catalyst. The purpose of the catalyst is to affect the reaction mechanism and therefore decrease the energy barrier without being consumed by the reaction[1]. Thus, the decrease in by-products and environmental impurities, resulting from the catalyst's impact, encourages the creation of sustainable and environmentally friendly products [1]. To achieve this demanding outcome, two types of catalysts are considered.
Heterogeneous catalysis is known for the catalysts being present in various phases in comparison to the reaction mixture. The catalyst is in the same phase as the reactant and product if homogeneous catalysis is considered. This form of catalysis is beneficial in reactions that require mild temperatures and pressures with precise molecular control [2]. Furthermore, this form of catalysis primarily involves transition-metal complexes, which exhibit high selectivity and activity even in asymmetric catalysis[3][4]. A metal complex is defined by a central metal atom accompanied by coordinated ligands that can vary in their backbone. Therefore, we consider homogeneous catalysis for this project.
A vital aspect in catalytic research is the concept of waste control and the use of raw materials converted into the storage of renewable energy, such as hydrogen. This molecule is characterized by its high energy density (119.9 MJ/kg), sustainability and abundance[5][6][7]. Homogeneous catalysis further influences hydrogen technology through the investigation of transition-metal complexes. Research on these complexes has led to identifying new hydrogen storage systems [8]. However, hydrogen storage is challenging as the hydrogen energy carrier has a low volumetric density (9.8 kJ/L) and needs enormous volumetric storage[7][9]. Long-established techniques, such as cryogenic liquid storage or high-pressure gas storage, require high infrastructure costs and are energy-intensive [8][9]. Therefore, alternatives such as liquid organic hydrogen carriers (LOHCs) are provided. LOHCs show promising behavior due to the large-scale storage and transport of hydrogen, which can be used for reversible hydrogenation and dehydrogenation[10][11].
The storage size can increase due to hydrogen's volumetric energy density when hydrogenation occurs, a process that is exothermic and typically occurs under moderate pressure (20-50 bar) and temperature (50-250°C) values [12], as seen in Figure 1.1. As hydrogenation reactions are hydrogen-dependent due to their cost-effectiveness and atom efficiency, they promote environmentally friendly processes that manage reaction rates and selectivity [13]. Dehydrogenation is an endothermic process that occurs mainly at atmospheric pressure, but in temperate conditions that increase to $420°C$ [12]. Thereby, a high heat demand could occur as extra hydrogen needs to be added to the system in the event that external heat is not available [14]. From the LOHC, the hydrogen atoms are added or eliminated, which is known as the substrate within the (de)hydrogenation reaction. The substrate is reversibly converted between hydrogen-rich and hydrogen-

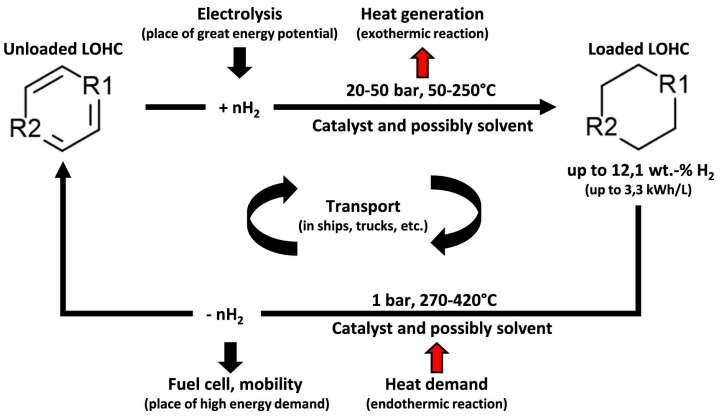

Figure 1.1: Schematic view of hydrogen transfer in dehydrogenation and hydrogenation reactions through LOHC [12]

poor states by breaking and forming chemical bonds [12]. Suitable candidates for LHOCs are N-heterocycles, which are characterized by their kinetics, thermodynamic stability, reversibility, and widespread availability with low vapor pressure [15]. Thus, dehydrogenation reactions with N-heterocycles are endothermic, avoiding unbounded thermal reactions and are processed with a decrease in enthalpy [16][6][10].
In general, we can assume that coordination of the N-heterocycle with the metal complex facilitates further reactions, including (de)hydrogenation reactions. Therefore, pyridine is chosen as a substrate, which is characterized by its stabilized aromaticity and the free lone pair positioned on the nitrogen atom. Together with pyridines π-donor property, it allows binding to the metal catalyst [17]. This interaction can impact the electronic property of the metal itself, determining the catalytic performance and stability of the various leading configurations of the metal complex.
Replacement of noble metal catalysts such as rhodium, platinum, or iridium is key as the catalytic performance can be more cheap and sustainable by implementing transition metals such as manganese [18]. This metal is known as the third most abundant element, consisting of various oxidation states ranging from -3 to +7 that differ from noble metals and enable it to engage in multiple chemical conversions, such as hydrogenation [19]. The Mn-based catalyst consists of two components: the metal center and its surrounding ligands. The combination of the metal and surrounding ligands results in a metal complex in which the ligands can bind in a mono-, bi- and tridentate manner. Binding occurs at one, two, or three different sites to the metal center. The tridentate ligands are defined as pincer ligands, which contribute to the performance and design of the catalyst. This type of ligand has proper control in how the coordination sphere surrounds the metal center as the donor atoms are arranged in a probable manner[20]. One type of pincer complex is seen, where the metal center is also surrounded by two auxiliary ligands, in this case the carbonyl molecule and a hydride atom that forms an octahedral complex in Figure 1.2. The activation of chemical bonds within this metal complex is determined mainly by the manganese (I) metal-ligand cooperativity mechanism (MLC) [19]. As the pincer ligand is validated to receive a proton after the dissociation of the dihydrogen molecule, the hydride atom can bind to the central metal atom, Mn(I), which is surrounded by the pincer ligand and serves as a hydrogen acceptor. Given this dihydrogen activation approach, the MLC enables the desired substrate to be hydrogenated by hydride transfer of the MnH species under benign conditions, serving as a LOHC technique, as seen in Figure 1.3. This mechanism is performed in two different environments. The inner-sphere mechanism highlights the hydride and proton transfer as the intermediate compound is formed, where the substrate remains bound to the metal-ligand complex [19]. This is the intermediate stage, before the substrate is fully saturated. The outer-sphere mechanism is proposed when no intermediate is present to immediately perform hydride and proton transfer to the unsaturated bond within the substrate [19]. The transfer of the hydride atom depends on the reactivity of the metal hydride bond and its free energy, known as thermodynamic hydricity[21]. The figure also demonstrates the active Mn(I)-PNP-based complex for the (de)hydrogenation of indole, as the products result in high chemo-selectivity and yields [16]. Other N-heterocycles, such as quinoline and imidazole, have recently shown promising catalytic behavior due to increased electron donation

and less steric constraint, especially for imidazole [22]. However, for (de)hydrogenation of the manganese(I)-based complex across various pincer ligands, pyridine was chosen as a model. Pyridine can be seen as one of the simplest compounds among all N-heterocycles with high aromatic stability [23], enabling further research on the binding and catalytic efficiency of the Mn-based complex. Manganese has shown promise in the field of catalysis through studies and experimentation with pincer complexes[13], which is the focus of this report.

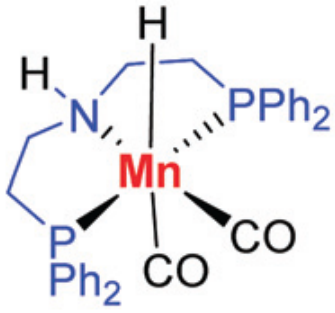

Figure 1.2: Manganese-based metal complex surrounded by PNP-pincer complex and auxillary ligands[19]

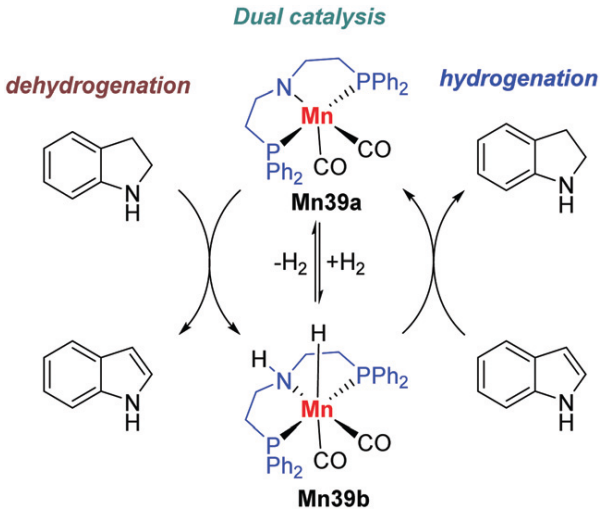

Figure 1.3: (De)hydrogenation mechanism of the Manganese-based complex[19]

Manganese-based complexes have shown promising results in catalytic research. Before 2016, Mn-based high-valent complexes were used for oxidative conversions focusing on bis(imino)pyridine (PDI) ligands that act as electron storage for the central metal to perform redox reactions involving two electrons, also maintaining the oxidation state of manganese [18][24][19]. In addition, alkene epoxidation reactions based on sustainable oxidants, such as hydrogen peroxide (H_2O_2), were performed successfully using NNN-pincer ligands[25]. Some attempts were made to achieve the activity in hydrogenation reactions. In general, the development of pincer ligands gained more recognition to improve metal catalyst performance, as PNP- or NNP-based ligands could promote the hydrogenation activity of Mn(I) for the reduction of organic compounds, such as ketones, aldehydes, or even N-heterocycles [26]. For example, the Kirchner Group showed improved progress toward the hydrogenation of aldehydes as the amount of reactant converted to product (TON) increased to 10400 for the neutral (PNP)Mn$(CO)_2$H(I) lutidine-based complex under mild conditions [19]. For ketones, an innovative approach was developed for the Mn (I)-based bidentate NHC-phosphine complex with low catalyst input and TON at 6200[19]. This led to the successful catalytic development of the Mn(I)-based PNC complex by Pidko's research group, which achieved a TON of up to 200,000 with KHBEt_3 as the base[19]. Specific base and pincer ligands are essential in increasing the catalytic activity of the complex[19]. However, applying these strong bases is often not feasible under mild conditions. Asym-

metric N-heterocycles could also be hydrogenated, as Lui's research group presented the Mn(I)-based NNP complex with the ferrocene compound as backbone[19]. From the N-H bond bound to the nitrogen pincer atom, the MLC mechanism is performed, resulting in the complex having high enantioselectivity, low catalyst input, and TON of 3840 [19].
The Mn-based PNP complex has also recently demonstrated its ability to perform acceptorless dehydrogenation reactions on challenging organic compounds, such as methanol [24]. Here, methoxide is formed by the removal of hydrogen without the use of an external hydrogen acceptor. This was carried out under the influence of a precatalyst such as $Mn(CO)_5Br$, which should be transformed into an active complex that undergoes the reaction with dihydrogen as it loses the bromide atom[19]. In addition, alcohols or even N-heterocycles can undergo coupling reactions after dehydrogenation. The PNP-Mn complex performed coupling by converting 2-aminobenzyl alcohols with another alcohol compound to quinolines (N-heterocycle) in high yield [24]. The latest study from the Liu group demonstrated high-performance in the hydrogenation reaction of imidazole in the NNP-Mn complex due to the high electron-donating property and minor steric strain of the N-heterocycle[22]. This successful complex behavior led to the development of an Mn-based complex with a bulky functional group bound to the nitrogen atom, which is coordinated to the benzo[d]imidazole compound (Figure 1.4) for the hydrogenation of 2-methylquinoline. Unfortunately, a low reactivity and yield of 21% was observed due to the assumption of sterics causing the ligand to block the binding of the bulky quinoline to the metal center[22].

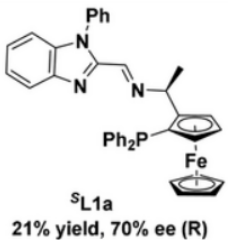

Figure 1.4: NNP-Mn pincer complex in the presence of the bulky functional group with a low yield of 21% [22]

Manganese, as a metal catalyst, has been used in the (de)hydrogenation reaction. With the promising characteristics of pyridine, it is key to investigate the catalytic behavior of the Mn(I)-based complex through the binding of this substrate. Specific types of ligands that consider both steric and electronic properties should be generated through computational screening, resulting in the development of Mn(I)-based ligands. The mentioned properties are essential to be controlled through the design of ligands to perform the MLC mechanism, which can influence the complex to be reactive [27]. Ligand design also introduces the concept of fine-tuning, for which specific substituents are varied to impact the electronic properties of bound pincer atoms [27]. However, recent studies have not yet thoroughly investigated the correlation between the ligand structure and the reactivity of the complex [26]. Hence, tuning the ligand design and creating a framework to forecast trends in reactivity that cover the metal catalyst are key for understanding the catalytic behavior of the metal.
This project investigates the behavior of some chosen phosphorus and nitrogen-based pincer ligands with CH_2- or O-linkers having various backbones that are accompanied by two auxiliary ligands (CO) and one hydrogen atom bound to the metal center (see Section 2.1). Reactivity comes into play because the complex contains a hydrogen atom, which is related to the hydricity of the metal-hydride species. Considering the specific metal complex, it facilitates coordination with LOHCs, such as pyridine, thereby enhancing hydrogen transport and storage. The interaction between pyridine and its potential to bind to the metal catalyst can impact the electronic properties of the metal itself, determining the catalytic performance and stability of the various leading configurations of the metal complex. In addition, the N-heterocycle-based LOHC mechanism is followed by homogeneous catalysis as it is processed with a decrease in the enthalpy of dehydrogenation [6][10].
Examining the catalytic behavior by synthesizing the different complexes and various catalysts would be time-consuming, challenging, and cost-intensive. Computational chemistry can therefore be applied to ex-

plore the synthesis of transition-metal complexes and to determine the reaction conditions under which the complexes are found to be stable. In the last twenty years, the field of in silico computational screening and design of coordination complexes for homogeneous catalysts has undergone significant development [28]. Thus, the paper of A. Kalikadien has reviewed the challenges, methods, and tools required for computational screening [28]. In silico high-throughput screening enables us to combine the metal catalyst with all ligand variants of the database to obtain the most beneficial contenders through DFT calculations [29]. In this project, high-throughput screening is performed to investigate whether the pincer ligands can stabilize this metal complex as well as to explore their potential use in N-heterocycles through ligand design. Hence, the focus in this report lies on the reactivity in comparison to the stability of the Mn(I) complex across various pincer ligands through in silico catalyst screening. This leads to examining the effect of the backbone on the catalytic activity of the complex with the identification of the ligand design and the possible fine-tuning of substituents, as computational screening is the new way to guide catalytic discovery.

1.2. Scope of thesis project

The purpose of the project is to investigate whether manganese-based complexes are thermodynamically favorable, with the metal being able to act as an active catalyst. The catalytic activity of Mn-based complexes is studied by focusing on the range of stable versus reactive complexes, taking into account the research questions that have been formed. First, all configurations are analyzed in terms of their stability in coordination with the substrate. The metal-ligand complexes that are thermodynamically attainable will be determined based on the electronic and steric properties of the various backbones described in our in silico library of ligands. Secondly, the reactivity is examined by investigating the charge distribution on the hydride atom for all complexes. We can then conclude which types of pincer ligands or configurations exhibit high reactivity based on the hydricity. Lastly, after the reactivity is analyzed, we examine how pincer ligands can be designed and what backbones can be utilized to fine-tune the interaction between the metal and the ligand.

2

Methodology

This chapter describes the computational and visual tools used in this research, which are executed in the order of the workflow. Different approaches for the specific tool within this workflow are highlighted by first addressing structure generation. Next, the visualization tool and its aspects are explained. Finally, the previous tools enable us to calculate the generated structures through the density functional theory via the ORCA software.

2.1. Standard library of pincer-complexes

To determine what type of metal catalyst complex results in an efficient and stable state to perform the catalytic hydrogenation process using density function theory (DFT) calculations, a standard library of various complexes is generated; see Figure 3.1.

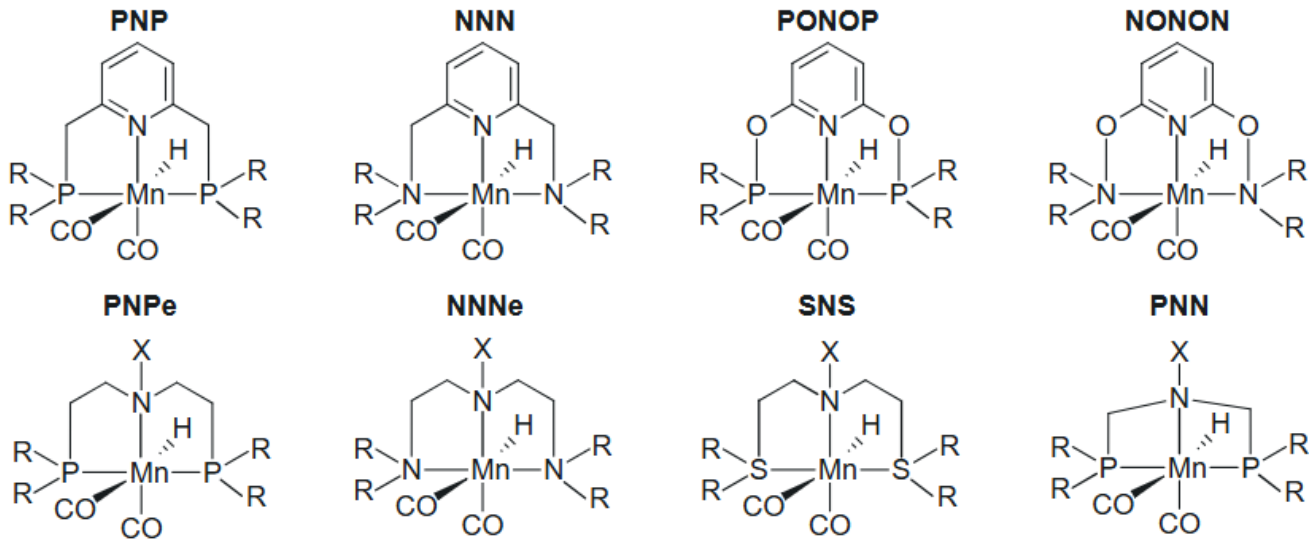

Figure 2.1: Database consisting of eight metal-pincer complexes with varying backbones

Each metal-ligand complex is associated with the following substituent groups:
R-group: Ph, tBu, Me, Cy, and iPr

X-group: H and Me

For further analysis, only the four metal-ligand complexes in the upper row are utilized because other complex structures are not properly converged by the provided structural generation and optimization tools, which are discussed in the upcoming sections.

2.2. Structural design

The high-throughput design of the selected pincer ligand structures, in combination with the metal catalyst and its auxiliary ligands, is discussed through the application of MACE and the ChemSpaX tool. DFT calculations are used in quantum chemical calculations to define the properties of the complex.

2.2.1. MACE and ChemSpaX

MACE is a computational method that constructs three-dimensional structures of all attainable stereoisomers for octahedral or square-planar transition metal complexes[30]. The input consists of two-dimensional metal complex structures that include the pincer ligands, the metal catalyst, and the auxiliary CO ligands (Figure 2.1). Pincer ligands are illustrated in a chemical editor tool known as ChemMarvin, which enables the generation of a SMILES code to represent the chemical structure of molecules [31]. After generating the appropriate stereoisomers, a Python package known as Open Bidentate Ligand eXplorer (OBeLiX) is used for expert-bias-free inspection of the stereoisomer [28]. This package further automates the design and workflow of stereoisomers by introducing ChemSpaX [28]. ChemSpaX further investigates the chemical space of possible catalytic structures by positioning substituents on pincer donor atoms [28]. This tool underpins the automated screening of metal-pincer ligand complexes as probable catalytic systems. The metal complexes were visualized by the advanced molecule editors, Avogadro and Chemcraft [32].
To initiate the hydrogenation reactions of our Mn(I)-based pincer ligand complexes, pyridine is viewed as our substrate model. This N-heterocycle serves as an LOHC, enabling investigation of the properties of the complex in terms of catalytic efficiency. The efficiency can be measured by the Gibbs free energy, which determines the thermodynamic favorability of the metal complex, ΔG, and is quantified by DFT calculations [33]. For each metal-ligand complex the total Gibbs free energy, $\Delta G_{\text{binding}}$, is calculated to examine the binding of the substrate and therefore the stability and activity of the Mn(I)-based complex. This is based on the following reaction:

$$\Delta G_{\text{binding}} = G_{\text{complex with pyridine}} + G_{\text{detached CO-ligand}} - G_{\text{complex}} - G_{\text{pyridine}} - G_{\text{reference pyridine binding}}$$

All parameters are quantified by performing DFT calculations to calculate the energetics, which will allow us to quantify the thermodynamics of the complex. The $\Delta G_{\text{binding}}$ holds for the pyridine to coordinate in a preferred geometry to the complex compared to the reference value for each backbone. The overall reaction now describes the replacement of the auxiliary carbonyl ligand by pyridine, thereby determining the binding energy of the ligand substitution relative to the most stable complex. This ligand replacement is crucial because substitution of the auxiliary carbonyl ligand with pyridine may not be successful, which in turn affects the stability of the complex. This assumption is observed in the ligand exchange for the $(Tianth-py_2)Mn(CO_3)Br$ complex, for which no reaction occurred or for which the auxiliary ligands were fully decoordinated [34]. The stability of the auxiliary CO ligand could be a proper indicator of the potential coordination of pyridine to the complex.
MACE has not generated the auxiliary CO ligand complex, as this computational workflow is a time-consuming process. A Python script was created to read each .xyz file containing its Cartesian coordinates. This enabled automation of replacing pyridine (Figure 2.2a) with an auxiliary carbonyl ligand, known as the reactant G_{complex} for which the phenyl group is placed in the backbone of the PNP ligand (Figure 2.2b).
To complete the reaction, the detached auxiliary CO ligand accompanies the product complex. The same principle holds for the reactant, for which the single pyridine compound is also present. This approach was applied to all ligands, including their substituents and backbones, to analyze the behavior of the substrate when entering the complex in terms of the stability and reactivity of the entire complex. Therefore, all ligand-

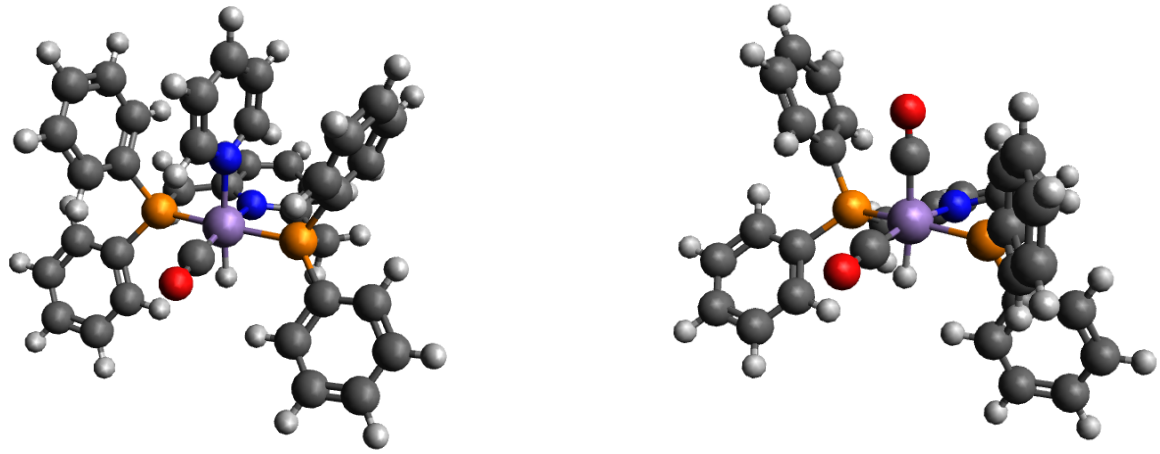

(a) (b)

Figure 2.2: Generated product and reactant structure for $\Delta G_{\text{binding}}$ computation. (a) Product: $G_{\text{PNPcomplex with pyridine}}$ with Ph as backbone. (b) Reactant: $G_{\text{PNPcomplex}}$ CO is substituted at the same position.

substituents are compared relative to the most stable configuration noted as ΔG_{ref}. This reference value is defined for each initial metal complex structure, not yet bound to the substrate, which has the lowest ΔG value for each ligand type within the backbone.

2.3. Density Functional Theory

To optimize geometry and perform frequency calculations for Mn(I)-based complexes across each type of ligand and its varying substituents, quantum chemical DFT calculations were performed with the ORCA 6.0 software and the supercomputer Snellius [35]. From the .xyz file, which contains the Cartesian coordinates of the pre-optimized transition complex, these coordinates are converted into an input file readable by ORCA. The input file also includes a basis set and keywords, which ORCA utilizes to define molecular orbitals for quantum chemical DFT computations in the gas phase [35]. The execution of the input file is run in parallel with 24 CPU bulks, each attaining 2500 MB of memory, at first. To improve the effectiveness and speed of execution, the number of cores was increased to 48 or 72. DFT calculations are performed using PBE0, an exchange-correlation functional that provides high accuracy and calculates the electronic properties of the metal complex [36]. In addition, manganese-based complexes have demonstrated accurate geometrical structures due to the use of PBE0 as a hybrid functional [37]. The exchange-correlation functional was accompanied by the dispersion correction keyword, D3BJ, which accounts for weak bonds, such as van der Waals interactions, to achieve chemical accuracy [38][39]. The basis set, def2-SVP, was executed, which polarizes the electrons on the atoms of the complex [40][41]. The presence of imaginary modes does not characterize the calculation of the vibrational frequency, as these modes could cause an inaccurate representation of the electronic structure[42]. The basis set and functional enable us to perform computations that result in the inner energy, enthalpy, and entropy and therefore the Gibbs free energy value. The final Gibbs free energy value takes place under the conditions of T= 298.15 K and P= 1.0 atm. Together with the Gibbs free energy, the electronic properties of all metal complexes are computed in the gas phase.

3

Results & Discussion

This chapter focuses on the stability and reactivity of various pincer ligands across all ligand backbones. The analysis evaluates the distribution of the Gibbs free reaction energy ($\Delta G_{\text{reaction}}$) which indicates a spontaneous process to form the pyridine-bound complex structures, the product, if a negative value is observed [43]. The configurations, the lengths of the metal-to-pyridine and carbonyl (auxiliary ligand) bonds, and the hydride charge distribution are also analyzed and discussed in further detail.

3.1. Gibbs free energy of reaction distribution

The variation of the functional group on the pincer arms has a profound effect on the coordination of pyridine and complex geometry. Figure 3.1 illustrates the $\Delta G_{\text{reaction}}$ distribution as a function of each pincer ligand substituent complex. Each complex with its various backbones is considered in three different configurations presented in Figure 3.2, in which the position of the carbonyl auxiliary ligand aligns with the hydride atom (configuration 1), pyridine (configuration 2) or lutidine part of the nitrogen-pincer arm (configuration 3). The complexes are present in an octahedral form and are mer-coordinated, which is distinctly favored by the pincer ligand [20]. Taking this into account, the absolute Gibbs free energies for each configuration across the ligand backbones are presented in Figure 3.1 relative to the most stable configuration of the starting complex, noted as the reference.

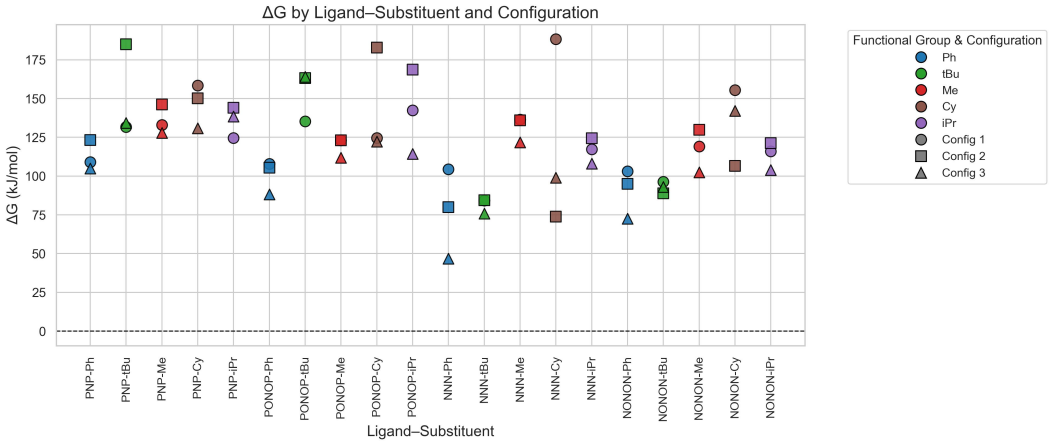

Figure 3.1: Gibbs free energy of reaction $\Delta G_{\text{reaction}}$ free energy distribution across each ligand-substituent and their configurations

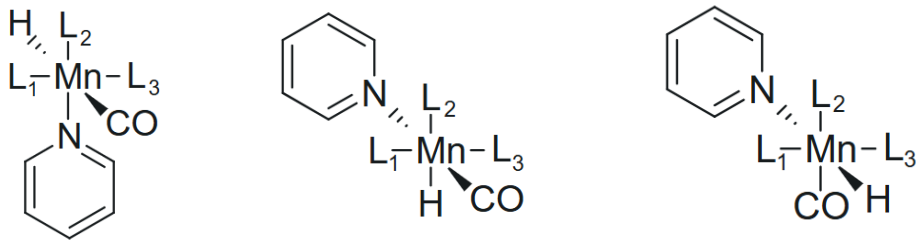

(a) (b) (c)

Figure 3.2: All possible manganese-based geometries illustrated as mer-$L_3MnH(CO)_2$. (a) Configuration 1: The carbonyl auxiliary ligand is trans positioned to the hydride atom. (b) Configuration 2: The carbonyl auxiliary ligand is trans positioned to the pyridine as substrate. (c) Configuration 3: The carbonyl auxiliary ligand is trans positioned to the L_2, which is the lutidine moiety, pincer N-atom coordinated to pyridine.

Across each ligand scaffold and their backbones, the phenyl-substituted systems provide relatively low $\Delta G_{\text{reaction}}$ values, especially for configuration 3, with the NNN type ligand having the lowest value being 46.8 kJ/mol. It is key to focus on the factors that define the clear preference for a particular configuration within each ligand type. The preferred geometry allows pyridine to fit nicely between the phenyl rings of the pincer arm substituents, providing additional stability because of π-π stacking [44]. This accounts for the third configuration for all ligand types as seen in Figure A.1. The second configuration shows less signs of π-π stacking in the NNN-based complex because the division in $\Delta G_{\text{reaction}}$ between both configurations is more pronounced relative to other ligand scaffolds. Another aspect that defines coordination is the electronic configuration; electronics can strongly influence the coordination geometry. This is mainly observed for almost all configurations for which the lowest $\Delta G_{\text{reaction}}$ values correspond to the auxiliary carbonyl moiety aligned with the lutidine part of the nitrogen-pincer atom (3.2c). The trans-positioning to pyridine (3.2b) for the nitrogen-based pincer ligands (NNN and NONON) is also sometimes observed. This alignment is favorable due to the orbital interaction that allows the π-donor, lutidine or pyridine, to align with the π-acceptor, carbonyl, thereby stabilizing the complex. The trans-positioning of the hydride atom to carbonyl, as depicted in 3.2a, causes no π-interaction due to the purely σ-donor property of the hydride atom, reducing complex stability. In addition, the nature of the pincer arm is also taken into consideration as the phosphorus atoms allow for stronger binding, which favors the alignment of the phenyl group, resulting in the third configuration being preferred. The nitrogen pincer arms, especially for the NNN-type ligand, allow weak binding but favor the alignment more in the presence of the phenyl substituent. Since the lowest value $\Delta G_{\text{reaction}}$ is observed for the third configuration, pyridine is most likely to bind to this nitrogen-based complex.

For the overall distributions, the dissociation of the auxiliary carbonyl ligand is unfavorable across all ligand scaffolds and their backbones, since no negative $\Delta G_{\text{reaction}}$ is observed. However, Ph-substituted systems seem the most favorable for all ligand-substituents. To further investigate the high likelihood of being favorable, the nature of the pincer arm is taken into consideration, as it has a profound effect on the potential configurational freedom of the complex. In the case of the phenyl substituent, the nitrogen-based ligand complex (NNN) allows high discrimination between geometries, ranging from 46.8 to 104.5 kJ/mol ($\Delta G_{\text{reaction}}$: 57.7 kJ/mol). Even for the challenging synthesized NONON-based complex, discrimination of the phenyl group is present for the third configuration relative to the first and second, although less pronounced than for the NNN ligand. In addition, clear discrimination is observed for the PNP-based complex between the phenyl groups and the other substituents. The Gibbs free reaction energy of the phenyl group ranges from 104.9 kJ/mol to 123.3 kJ/mol, while the other substituents range between 124.5 kJ/mol (iPr, configuration 1) and 185.1 kJ/mol (tBu, configuration 2), thus a $\Delta G_{\text{reaction PNP diff}}$ of 60.6 kJ/mol. This observation also accounts for the PONOP-based ligand for which the Gibbs free reaction energy ranges between 88.3 kJ/mol and 107.9 kJ/mol, with the third methyl configuration starting from 111.8 kJ/mol to 182.9 kJ/mol ($\Delta G_{\text{reaction PONOP diff}}$: 71.1 kJ/mol). Thus, the substitution of the CH_2-linker with the rigid O atom shows an increased discrimination pattern between the phenyl geometries and the other functional groups within the ligand scaffold. This could indicate that the PONOP-based complex prefers the Ph-substituted system more compared to the

PNP-based systems. The NNN-based complex shows, by far, the preferred environment for the phenyl backbone to coordinate to the complex due to the lowest binding energy and the electronic alignment of the third configuration.
The PNP-based complex illustrates for the bulky tert-butyl group a wide $\Delta G_{\text{reaction}}$ energy distribution range, from 131.7 kJ/mol to 185.1 kJ/mol. At the same time, this discriminating property is present but less pronounced in the PONOP ligand type. In addition, the rigid oxygen linker atom combined with phosphorus-based pincer arms (PONOP) allows the binding energies of two configurations to collapse to approximately the same place in a higher energy range which is more pronounced than for PNP ($\Delta G_{\text{reaction, PONOPconf2-3}}$: 163.31 kJ/mol - 163.99 kJ/mol, $\Delta G_{\text{reaction, PNPconf1-3}}$:131.1 kJ/mol - 134.4 kJ.mol). Both ligand types favor the first configuration with the lowest Gibbs free energy value, indicating that the complex is less stable and is amplified by the steric effect of the tert-butyl group. Configurations 2 and 3 are entirely unfavorable due to their molecular structures, which were obtained after geometry optimization. The bulky environment causes the auxiliary carbonyl ligand to bend, disrupting orbital alignment, which is illustrated for both the PNP ligand type and the second configuration in the PONOP ligand scaffold, as viewed in A.2. The third configuration is influenced by the dominance of steric effects and the rigid oxygen atom rather than the electronic alignment of the lutidine part of the pincer with the auxiliary CO ligand. However, the tert-butyl complexes are mainly distributed within the same bulk for the NNN and NONON pincer-type ligands. The nitrogen pincer ligand, with its flexible CH_2-linkers, even forces the entire complex to be in a lower energy range (75.8 kJ/mol - 84.4 kJ/mol) compared to the other ligand scaffolds. As the configurational energies are clustered together, no particular geometry could be excluded, especially for the NONON-based complex. This would result in no clear identification of the effect of steric hindrance on a specific configuration that needs to be considered when designing ligands. As no specific configuration is observed, the presence of steric hindrance leads to side coordination. Figure A.3 represents the side coordination for complexes based on NNN, NONON, and PONOP pincer ligands, for which the NNN type mainly shows the bulky groups pointed sideways. Therefore, the nature of the pincer arm and its linker has a profound effect on the potential configurational freedom of the tBu-substituted systems. It could be stated that the weak binding of the nitrogen atom with tert-butyl explains the occurrence of the configurations within the same bull park compared to the strong binding of the phosphorus with tert-butyl. The rigid oxygen within the PONOP and NONON ligand types causes the clustering of configurations; thus, the NONON-based complex is the most affected. In addition, the steric hindrance of the bulky group causes the preferred third configuration to exhibit greater instability, as bending of the CO bond is observed. This results in a higher energy level compared to its NNN-based counterpart that views slightly more bending of the CO bond (A.3f). The firmly bound phosphorus-pincer ligands with the oxygen linker exhibit increased unfavorability, as the same configuration is plotted at a higher energy level compared to the nitrogen-based complexes. Thereby, less bending of the auxiliary ligand is observed (A.3i), compared to PNP (A.2b). This suggests a more rigid system as it is influenced by the steric hindrance of the tert-butyl group rather than the bending of the auxiliary carbonyl ligand. The strongly bound phosphorus atom with the rigid oxygen linkers amplifies this influence due to the high ligand binding energy observed ($\Delta G_{\text{reaction, PONOPconf3}}$: 164.0 kJ/mol > $\Delta G_{\text{reaction, PNPconf3}}$: 134.5 kJ/mol).
Although cyclohexane is expected to be extremely bulky and comparable to tert-butyl, the figure 3.1 contradicts this. Both cyclohexane and isopropyl show clear discrimination patterns across all types of ligands in the energy distribution, with no intense clustered forms visible in the nitrogen-based complexes. These groups find a configuration that does not restrict the coordination of the pyridine with the metal center. For example, the cyclohexane substituent clearly illustrates the highest first configuration, $\Delta G_{\text{reaction}}$: 188.3 kJ/mol, depending on the NNN ligand scaffold. The nature of the pincer atom could explain this, as its weak binding forces the large environment of the substituent to hinder the hydride atom of the Mn-based complex, which is more noticeable than for the other two configurations (A.4). The isopropyl functional group exhibits the most discriminative behavior in the PONOP ligand type. The unfavorability of these two groups is most pronounced in their second configuration, with the highest $\Delta G_{\text{reaction}}$ value for the PONOP ligand scaffold. Just as observed for the exact configuration and ligand type in the tert-butyl backbone, the large environment results in bending of the auxiliary carbonyl ligand A.5a. The dominance of steric effects rather than the electronic alignment of the pyridine with the auxiliary CO ligand is hereby the main factor.

The methyl group exhibits an energy distribution for each ligand scaffold within a narrow range, with the PONOP type at a lower energy range compared to the higher energy range of the PNP type. Across all ligand types, the second configuration always illustrates the highest energy value as it is impacted by clear bending of the auxiliary ligand A.6. Therefore, its small environment does not relate to the preferred orbital interaction between the pyridine and the auxiliary CO bond, which prevents stabilization of the complex. Although the third configuration yields the lowest binding energy across the backbone, no clear preference is observed for replacing the carbonyl moiety with pyridine because of the relatively high binding energies.
Together with the properties of the bulky and large groups, the NNN(Cy, Ph) and PONOP (tBu, Cy, iPr)ligands are influenced by the system's sensitivity to variation in substituents. This allows for possible selective fine-tuning of the complex properties. However, further analysis will confirm which ligand scaffolds contribute to fine-tuning the properties of the ligand. The Ph-substituted system is preferred across all ligand scaffolds, especially the NNN-based complex. Therefore, it can be assumed that for the other substituents across all ligand types likely perform an outer-sphere mechanism for the (de)hydrogenation of pyridine. This mechanism involves the transfer of proton and hydride without consistently coordinating pyridine stably to the complex[19]. If the phenyl group is considered to be favorable compared to the other backbones and ligands, it could undergo the inner sphere mechanism. Stable intermediate species support this mechanism, the Ph-substituted system across each ligand type, focusing on the third configuration of NNN-Ph [19]. However, the positive binding energies could contradict this observed mechanism. The high likelihood of stability within this complex and across its ligands and substituents prompts further investigation by studying the difference in the Gibbs free energy of the reaction relative to the most stable initial complex structure across each backbone.

3.2. Properties of initial Mn-based complexes

After evaluating the behavior of pincer ligand complexes across various backbones, we further investigate whether a trend is observed in which metal complexes favor one type of configuration or exhibit configurational flexibility. Each configuration resulting from the ligand-substituent configuration is expressed as $\Delta G_{\text{reaction}}$ relative to the most stable initial configuration structure with the lowest energy value, presented in Figure 3.3. Cyclohexane illustrates obvious discriminating behavior with phenyl and tert-butyl also potentially showing division between the configurations across the PNP-based complex. The isopropyl substituent illustrates a clear flexible behavior as two configurations are within the same bulk. The methyl group tends to behave somewhat similarly to the isopropyl functional group. When we delve further into detail, the Boltzmann distribution weight is taken into account, which calculates the relative weight of each configuration within the ensemble across each backbone. To confirm our observation, the following formula is applied [45]:

$$w_j = \frac{e^{-Ej/(k_B T)}}{\sum_j e^{-Et/(k_B T)}}$$

for which:

- w_j is the standardized weight (%) related to each configuration j,
- E_j is described as free energy, in particular Gibbs free energy of reaction (kJ/mol) of the initial Mn-based complex related to each configuration j,
- E_t is described as free energy, in particular the total Gibbs free energy of reaction (kJ/mol) corresponding to all configurations within the backbone,
- k_B is described as the Boltzmann constant (8.617×10^{-5} eV/K),
- T is described as the temperature in Kelvin (298.15 K),

The weight value for each configuration is calculated and illustrated in A.1. Our observation is confirmed

because phenyl, cyclohexane, and tert-butyl contribute a weight value of 99.9 % to the third configuration, which is therefore the preferred geometry. The methyl group still prefers to accommodate the first configuration as a w_1 of 92.4 % is observed. Isopropyl confirms the flexibility of the two configurations as the first has a w_1 of 47.9 % and configuration 3 has a w_3 of 52.1 %. This illustrates that the first configuration prefers to engage in the unbound-pyridine coordination sphere, which is not the stable third configuration chosen as the reference. This is confirmed by the fact that this configuration has the lowest Gibbs free reaction energy when pyridine binds to the complex, as shown in 3.1. The bulky environment explains why alignment of the carbonyl compound with the hydride atom is preferred and is even confirmed by the increased steric effect of tert-butyl, which also selects this configuration (3.1).
The PONOP-based complex indicates clear flexibility of configurations 1 and 3 for the phenyl, tert-butyl and methyl substituent. However, the first configuration contributes slightly more to all three functional groups, as the weights for phenyl are :w_1: 51.0 % and w_3: 49.9 %. Cyclohexane illustrates discriminating behavior as the first configuration is the most preferred, w_1: 99.1 %, while the third configuration occurs much less frequently, w_3: 0.9. The reverse trend for isopropyl is observed as the weight values of both configurations are w_3: 99. 9 % and w_1: 0.1 %. Flexibility is more observed in this ligand scaffold compared to the PNP-based complex, for which the reference structure (configuration 1) of the phenyl and tert-butyl groups is accompanied by the third configuration. After geometry optimization of the pyridine-bounded structure, the third configuration is considered to be preferred, as the lowest $\Delta G_{\text{reaction}}$ belongs to phenyl and even the large cyclohexane, seen in 3.1. However, tert-butyl still prefers the first configuration, which is plotted even higher in Gibbs free reaction energy than the phenyl substituent. This indicates its instability and high impact of steric hindrance, which is also observed for the PNP ligand scaffold.

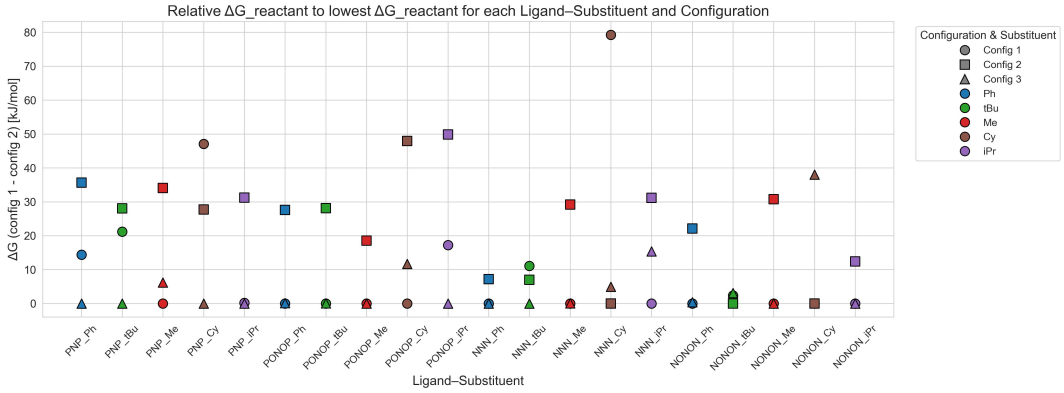

Figure 3.3: Gibbs free energy $\Delta G_{\text{difference}}$ between configurations relative to the most stable initial complex structure across each backbone and ligand scaffold

The most significant variety in weight distributions is presented in the NNN-based complex. Similarly to the PONOP-based complex, the phenyl and methyl groups again exhibit flexibility for configurations 1 and 3. In particular, phenyl equally favors both configurations w_1 and w_3: 48.7 % and methyl prefers configuration 1 slightly more w_1: 50.6 %. Both functional groups were plotted relative to their stable configurations, the third for phenyl and the first for methyl. Tert-butyl appears to show flexible behavior as a short range is observed, yet the third configuration is the most preferred w_3: 93.3 %. Cyclohexane exhibits clear discriminatory behavior, with configuration 1 being the least preferred and configuration 2 being the most dominant (w_2: 87.9%). Isopropyl favors configuration 1 as the weight value is w_1: 99.8 %. Following the weight distributions of each backbone, the pyridine-bound structures (3.1) still prefer the third configuration, which deviates from the methyl and isopropyl substituents that illustrated larger weight values for configuration 1. The side-coordinated, bulky tert-butyl group even favors this configuration, deviating from that of the phosphorus-based complexes. The other large groups, such as cyclohexane, prefer the second configuration. This suggests that the substrate favors the alignment of the auxiliary CO ligand with both the lutidine part of the pincer and the pyridine compared to the phosphorus-based complexes.
The least discriminative configurational behavior is most significant in the NONON-based complex. Tert-

butyl exhibits distinct configurational flexibility for which configuration 2 is more preferred: w_1: 22.9 % , w_2: 60.6 %, and w_3: 17.1%. The other groups show configurational freedom for two configurations, again for phenyl w_1: 53.8 % and w_3: 46.2 %. However, after geometry optimization, all backbones favor mainly the third configuration, as observed in the NNN-based complex.
In general, configuration flexibility depends on the nature of the pincer atom and its linker. The firmly bound phosphorus atom, with rigid oxygen linkers (PONOP), promotes more configurational flexibility for three of the five groups compared to its PNP counterparts. However, phosphorus-based complexes indicate the configurational preference for an unstable geometry (configuration 1) in the case of the bulky tert-butyl group when pyridine is bound to the complex. For the initial and pyridine-bound structures of the NNN-based complexes, configurational flexibility as well as geometric preference can vary depending on the ligand backbone. Therefore, nitrogen-based complexes with CH_2-linkers could contribute as a candidate for the design of ligands, as they are affected by high sensitivity through changes in the backbones [46]. The NONON ligand scaffold exhibits the most prominent flexibility across all of the backbones. Combining the weak-binding nitrogen pincer arm with the rigid oxygen atoms could also enable the design of ligands. This is assumed but is further investigated in this study.
In terms of the stable phenyl group, the fine-tuning of ligands is mainly dependent on the type of pincer atom and the linker. This is suggested by the high sensitivity observed for all ligand types for its pyridine-bound structures, except for the PNP-based complex (3.1). This observation is confirmed by the initial structures, which illustrate greater configurational flexibility relative to each configuration of the PNP ligand scaffold, as seen in 3.3. Understanding the preferences between each type of ligand, based on $\Delta G_{\text{reaction}}$, is key to further examining how the various substituents can affect geometry when considering the distance between the substrate and the metal, as well as for the carbonyl auxiliary ligand of the metal.

3.3. Gibbs free energy of reaction vs bond length

To observe a correlation between the energy distribution and the length of the metal pyridine bond for stable and less stable complexes, the figure 3.4 is plotted. No clear trend is observed, as a diverse spread of binding energies is seen at various lengths of metal-pyridine bonds for the bond length range between 1.95 Åand 2.20 Å. This observation does not correlate with the hypothesis for which an increase in $\Delta G_{\text{reaction}}$ could explain a relatively long metal-pyridine bond that instigates weak binding of the substrate within the complex. To identify and assume a standard range of the length of the metal-pyridine bond, figure A.8b is used for which most lengths are set between 2.00 Åand 2.10 Å. Therefore, the phenyl (2.113 Å, configuration 3) and tert-butyl (2.174 Å, configuration 2) substituents from the NNN-based complex are considered too long. This also accounts for the whole tert-butyl complex of NONON, in which configurations 1, 2, and 3 have bond lengths of 2.124 Å, 2.154 Å, and 2.142 Å, respectively. Some configurations, which are assumed to be short and therefore absent from the standard range, are cyclohexane (configuration 3, 1.973 Å) and isopropyl (configuration 3, 1.966 Å) of the NNN-based complex. The methyl backbone (config 1, 1.993 Å), cyclohexane (configuration 3, 1.986 Å), and isopropyl(config 3, 1.988Å) are also included, which belong to the NONON-based complex. It is also key to consider the bond length between the metal and the auxiliary carbonyl bond of the bound pyridine structure for every configuration, as seen in Figure A.9. These two bond length properties could be helpful, as our second hypothesis indicates that the bond strength of the metal-pyridine bond is favored if the Mn-CO bond elongates as it faces weak π-backbonding [47][48].The standard range is defined between 1.73 Åand 1.766 Åfor which the phenyl substituents appear to have long Mn-CO bonds for its first configurations for NNN (1.790 Å) and NONON (1.782 Å). The PONOP-tBu (configuration 2, 1.729 Å), PONOP-Cy (configuration 2, 1.727 Å) and NONON-tBu (configuration 2, 1.728 Åand configuration 3, 1.727 Å) are considered to have short Mn-CO bond lengths. Surprisingly, the longer metal-carbonyl bonds appear for every first configuration across all ligand-substituents. Thereby, as the second configuration accommodates a hydride at the equatorial position, a longer Mn-CO should be observed. However, the second and third configurations are primarily for phenyl groups in a close range across all ligand types. We will further investigate this effect on the stable and less stable configurations.
The most stable configurations are determined only by the phenyl substituent, as its π-system can delocalize

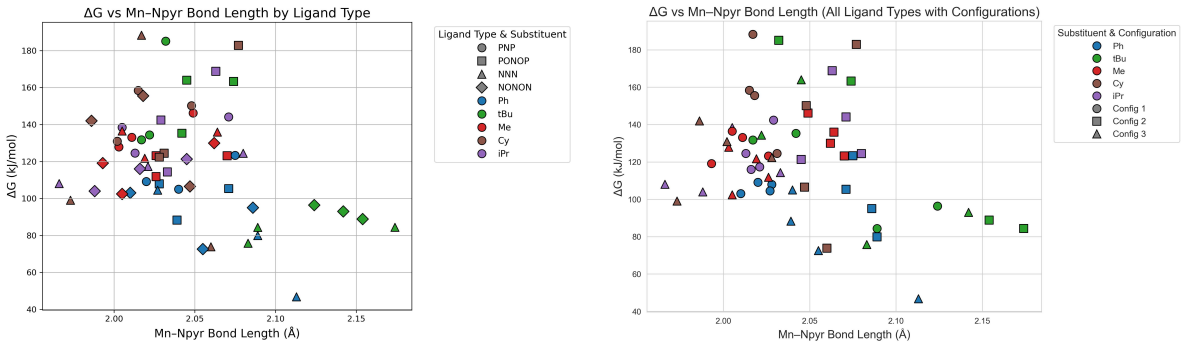

(a) (b)

Figure 3.4: Energy distribution in terms of $\Delta G_{\text{binding}}$ as function of the manganese pyridine bond length. (a) Energy and bond length distribution across different ligand types and their substituents. (b) Energy and bond length distribution across the substituent and its configuration.

the electrons to cope with geometric hindrance across the conformations. Figure 3.4 shows that configurations 2 and 3, for all ligand types, decrease in Gibbs free reaction energy when the length of the Mn-Npyr bond increases. Focusing on the standard bond length range between 2.00 Åand 2.10 Å, the third configuration is shorter than the second configuration in each ligand scaffold, except for NNN. This deviation belongs to the third configuration which exhibited the most favorable behavior as illustrated in Figure 3.1 due to its lowest Gibbs free energy of reaction. Thereby, a moderate Mn-CO bond length is observed for both configurations, which are in the standard range between 1.73 Åand 1.762 Å. Overall, the third configuration exhibits relatively weak Mn-Npyr bond lengths, as it falls outside the standard range. The first configuration of the phenyl substituent falls within the standard Mn-Npyr range, which applies to all ligand scaffolds. However, the Mn-Npyr bond is relatively shorter (2.027 Å) than the preferred second and third configurations, as observed in Figures 3.4 and A.8b. Thereby, extreme outliers in the Mn-CO bond length are observed only for the first configurations of the nitrogen-based complexes. This suggests that for determining the complex stability and configurations, the bond lengths between the metal and the pyridine and carbonyl ligands do not correlate with our preferred alignment of the carbonyl auxiliary ligand with either pyridine or lutidine. This also accounts for the first configuration, for which we can conclude that our two hypotheses are contradictory. Thus, these bond lengths are not representative for the analysis of the stability of these phenyl-related complexes in terms of the binding energy.

To examine whether the correlation between the binding energy and the metal-pyridine bond length is inconsistent, we considered the less stable complexes and their configurations. The third configuration occurs in the range between 1.95 Åand 2.05 Åof the energy distribution relative to the metal-pyridine bond length in figure 3.4. From 2.00 Å, the first configuration is observed frequently, after which the second configuration occurs mainly from 2.05 Å. Tert-butyl deviates from the overall crowded region, as the high-energy values are plotted even in the increased bond length range of 2.10 Å to 2.20 Å for the nitrogen-based complexes. From the NONON-based complex, all three configurations were considered to have very long metal pyridine bonds, outside the standard range as seen in figure A.8b. The steric tert-butyl group compensates for its very long metal-pyridine bonds by very short Mn-CO bond lengths, outside the standard range, for the second and third configurations(figure A.9). This observation indicates that the alignment of the auxiliary CO ligand with the lutidine part of the pincer atom or pyridine is less favorable. Therefore, since all configurations were present within the same bulk and were even in a moderate energy range relative to the other backbones (figure 3.1), no particular configuration could be preferred. This is due to the instability of all configurations, as could be confirmed by the relatively moderate to high Gibbs free energy of reaction and the presence of both long metal-pyridine and short metal-CO bonds, seen in figure 3.4. For the NNN ligand type, which also illustrates the same bulk, the second configuration illustrates the most extended Mn-Npyr bond length (2.174 Å). This is compensated by a relatively short Mn-CO bond (1.733 Å). Interestingly, the first and second configurations accommodate almost the same energy but vary in bond length for the NNN-based complex.

This indicates that configurational freedom is dependent on binding with pyridine rather than on bulkiness. Based on this observation, the first configuration is assumed to be preferred, as the Mn-Npyr bond length is relatively shorter and the Mn-CO bond is longer; however, this confirms again the unreliability of the correlation between the binding energy and the bond lengths due to the unfavorable nature of this alignment. The same is observed in the PONOP type ligand for configurations 2 and 3 at very high binding energies, even though the third configuration has a shorter bond length for Mn-Npyr compared to configuration 2 within the standard range (2.00 Å- 2.10 Å). Therefore, the alignment of these configurations is also not preferred. Another observation within this type of ligand is that various energy values are distributed against similar bond lengths in the range between 2.00 and 2.05 Å. This accounts for the third configuration which has a higher $\Delta G_{\text{reaction}}$ of 163.9 kJ/mol compared to the first configuration with $\Delta G_{\text{reaction}}$ of 135.3 kJ/mol. As the third configuration is even less preferred because of its high binding energy, this suggests that the configurational energies are not influenced by the binding of the substrate, but rather by its confirmed steric hindrance. The PNP ligand scaffold illustrates the highest energy value ($\Delta G_{\text{reaction}}$:185.1 kJ/mol) compared to the other tert-butyl backbones, which disfavors the alignment of the auxiliary carbonyl ligand with pyridine. Both configurations 1 and 3 accommodate the same energy range but differ in the Mn-Npyr bond length, as the first configuration is slightly shorter. This suggests configurational freedom for the complex, for which the first configuration would be preferred. Yet, this configuration is not preferred due to its unfavorable electronic alignment. Tert-butyl could lead to instability because of the impact of steric hindrance and the unfavorable electronic alignment of the configuration observed across each ligand scaffold.
Cyclohexane, isopropyl and methyl also deviate from the crowded region, as they are present in the very short Mn-Npyr bond length range between 1.95 Å and 2.00 Å for the nitrogen-based complexes. This region encompasses all third configurations for the cyclohexane and isopropyl substituents, illustrating the shortest Mn-Npyr bond length associated with the NNN-ligand type. The NONON-ligand shows a slight increase in bond length for its cyclohexane and isopropyl functional groups. This is also applicable to the methyl functional group, for which the first configuration is illustrated. All configurations have similar moderate Mn-CO bond lengths (1.75 Å). Even for this third configuration, for which strong pyridine binding could occur, instability is observed because of the high-energy distribution ranging from 99.0 kJ/mol ($\Delta G_{\text{reaction, NNN-Cy conf3}}$ to 142.0 kJ/mol $\Delta G_{\text{reaction, NONON-Cy conf3}}$. Thus, the correlation between binding energy and bond lengths is again not observed for these groups. Even at a similar bond length between iPr-NONON and Cy-NONON (1.986 Å-1.988 Å), the configurational energies are dependent on the bulkiness rather than on the binding of pyridine. Thereby, it would indicate that cyclohexane is more influenced by steric hindrance, making the third configuration less favorable. This also accounts for the first configuration as Cy-NONON still accommodates a higher binding energy due to the larger steric environment of cyclohexane than for isopropyl when the Mn-Npyr bond length increases (2.016 Å- 2.018 Å). Surprisingly, this observation changes when for similar metal-pyridine bond lengths at a higher range (2.045 Å- 2.047 Å), the second configuration of Cy-NONON has a lower binding energy compared to iPr-NONON. This indicates a preference for the electronic alignment of the auxiliary carbonyl ligand with pyridine over the impact of the larger hindered environment of the cyclohexane substituent. Thus, the steric effects dominate the electronic alignment of the configuration when a relatively shorter Mn-Npyr length is observed. To investigate if the same pattern with similar bond lengths is present for the NNN-ligand type, we could only observe the methyl group as a comparison instead of the isopropyl substituent. It could be assumed that the methyl and isopropyl groups are less sterically hindered than the cyclohexane substituent and, therefore, could be used as a measurement. Interestingly, the high influence of steric effect changes as the bond length increases when the second configuration of Cy-NNN has a $\Delta G_{\text{reaction}}$ of 73.9 kJ/mol compared to the second configuration of Me-NNN with a $\Delta G_{\text{reaction}}$ of 135.9 kJ/mol at quite similar bond length values (2.060 Å- 2.064 Å). This indicates a preference for the exact alignment (configuration 2) over the impact of the large cyclohexane substituent environment, compared to the small methyl functional group. The weak nitrogen pincer atoms can relieve the steric strain upon coordination, a phenomenon also observed in the nitrogen-based complex with its rigid oxygen linkers. Therefore, the nitrogen-based complexes prefer the electronic alignment of the second configuration over the impact of the steric hindrance induced by the large cyclohexane when comparing less steric groups. Overall, these three substituents exhibit less stability, as both their steric and electronic effects contribute to this.

The instability of these groups is more pronounced for the phosphorus-based complex between 2.00 Åand 2.10 Å, for which we focus on the PONOP ligand scaffold. Figure A.10 focuses on each separate ligand scaffold of which PONOP illustrates the second configuration of cyclohexane to be the highest in binding energy, $\Delta G_{\text{reaction}}$: 182.9 kJ/mol. Bending of the auxiliary CO ligand amplifies the weak binding of the substrate, confirming its instability A.7a. Here, the short Mn-CO bond (1.727 Å) does not correlate with the moderate length (2.077 Å) observed, again contradicting our hypothesis about the two bond lengths. The first and third configurations have nearly the same Gibbs free energy of reaction, with the third one being slightly shorter for the metal-pyridine bond length. Still, no clear distinction is observed to consider the third configuration to be more favored. The second configuration of the isopropyl substituent is also in a higher energy range of $\Delta G_{\text{reaction}}$: 168.8 kJ/mol, which is still unfavorable due to the same bending observed of the auxiliary ligand as for cyclohexane A.5a. Configurations 1 and 3 depend on the bulkiness of the substituent, as almost the same bond length is observed (2.029 Å- 2.033 Å), indicating the high steric impact when the auxiliary carbonyl compound aligns with the hydride atom. Configuration 3 faces less of this impact, as it is at a lower energy level ($\Delta G_{\text{reaction}}$: 114.3 kJ/mol). The methyl substituent exhibits the same binding energy for configurations 1 and 2, with the first conformation displaying a significantly shorter Mn-Npyr length. The configurational preference is again shown for the trans-positioning of the auxiliary carbonyl ligand with the hydride atom, which is unfavorable. The second configuration faces, just as for the other substituents, bending of the auxiliary ligand that results in unfavorable orbital alignment A.6b.The third configurations of all three substituents are even clustered in the same energy region. However, they are characterized by the bending of the auxiliary CO ligand toward the hydride atom, resulting in disruption of orbital alignment with unfavorable binding energies, as seen for all three substituents (A.7b,A.7c, A.7d). Thus, it is observed that all groups face less stability in their complex and specific configurations because of the unfavorable binding energies and the disruption of orbital alignment. The correlations between the binding energy and metal-pyridine bond, and also the two bond lengths (Mn-Npyr and Mn-CO), are irrelevant to conclude the weak binding of the metal and pyridine for these unstable complexes. However, it would be relevant to investigate whether the reactivity of the complex is affected.

3.4. Reactivity

To take into account the reactivity of the complexes, we further investigate the impact of the ligand binding energy on the properties of the Mulliken hydride charge. Two different visualizations are considered. First, the binding energies of the ligand-substituent as a function of the hydride charge of the pyridine-bounded complex across each substituent and its configurations, illustrated in Figure 3.5. Secondly, the charge of the hydride as a function of each pincer ligand and its functional group in their reactant and product form, shown in Figure A.12. This figure emphasizes that, for almost every ligand-substituent, the hydride distribution of the initial complex structure (CO-reactant) is higher than that of the pyridine-bound structure (Pyr-product) due to its electron-withdrawing characteristic. In figure 3.5, it is observed that nitrogen-based complexes provide the highest negative charges for their first configuration across all backbones, ranging from -0.295 e to -0.353 e. In terms of the most stable configurations, the third configuration exhibits the highest reactivity for the Ph-NONON-based system (-0.228 e), followed by Ph-NNN, which exhibits the most negative hydride charge (-0.216 e). The second configuration exhibits more negativity, with a value of -0.231 for Ph-NNN and even -0.266 e for Ph-NONON. The third configuration for nitrogen-based complexes falls within the range of -0.250 to -0.200 e. Both phenyl-based configurations show the most negative hydride charge value for the nitrogen-based complexes compared to those of other ligand types and even their backbones. This also accounts for the phosphorus-based complexes. Overall, this could correlate with our third hypothesis, which suggests that for higher negative charges, the reactivity of the complexes plays a significant role for activating the pyridine-bound complex. Reactivity is therefore key to enhancing the activity of the configuration, as mainly the nitrogen-based complex improves the nucleophilicity of the hydrogen atom of the metal complex [26]. This could positively impact the hydricity of the complex. However, the metal complexes are unable to participate as active candidates, as the positive binding energies do not correlate with the hydridic configurations observed, especially for the nitrogen-based complexes. Therefore, further hydrogenation could not

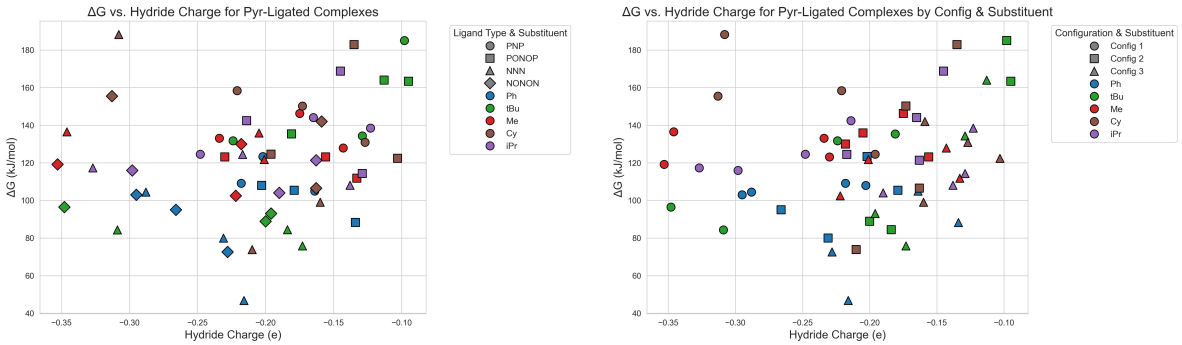

(a) (b)

Figure 3.5: $\Delta G_{\text{reaction}}$ energies distributed against the hydride charge in terms of reactivity. (a) Distribution of energy plotted against each pincer ligand type with the functional groups. (b) Distribution of energy specifying each configuration across all ligand types and backbones.

be realized as this suggests that all complexes perform through outer-sphere mechanisms.
From the graph, as the hydride charge becomes more positive, the configurations switch from the first to the second, after which the third configuration mostly occurs. The nature of the pincer arm and its linkers is also dependent on the occurrence of negative hydride charge values. The nitrogen-based complexes seem to be more present in the higher negative charge range, especially for the first configuration. The methyl group exhibits the most negative hydride charges, for which the NONON ligand scaffold is more pronounced than the NNN ligand type. Unlike the phenyl group, the methyl group is an electron-withdrawing group, which is not able to donate electrons to the metal center when the auxiliary carbonyl ligand and the aligned hydride atom engage to receive electrons from the metal. Furthermore, rigid oxygen linkers exhibit good electron-donating ability. Therefore, the combination of the weakly bound and electron-rich pincer atom with its rigid oxygen atom and the electron-poor substituent could validate the very negative hydride charge, providing electron density to the metal center [26]. This also accounts for the other backbones, which all exhibit less electron-withdrawing ability. High negative charges also occur for the nitrogen-based complex, though less frequently due to its flexible CH_2-linkers. However, we would expect the binding energy to be much lower as a result of this electronic compensation, which is not the case. Therefore, it could not be concluded that high reactivity correlates with the stability of the complex.
For phosphorus-based complexes, the first configurations provide a decrease in negative charges, which is more pronounced for the PONOP-based complex, as seen in Figure A.11b. Almost all second and third configurations occur in the lowest hydride charge region of -0.15 to -0.10 compared to their PNP counterparts. This is determined by the nature of the pincer arm and its linker. The phosphorus pincer atom has a profound effect on the reactivity of the complex when bound to the rigid, electron-donating property of the oxygen atom. The less nucleophilic character of the phosphorus atom forces all configurations to have relatively less reactivity, even when bound to the rigid oxygen atom. The PNP-based complex exhibits a more pronounced spread toward negative values (A.11a), while the NNN-based complex displays a more diverse pattern (A.11c).
Just as for the NONON-based complexes, the weak nitrogen pincer atoms in the NNN-based complex exhibit a diverse pattern in hydride charges and binding energies across all configurations, for each backbone. In particular, for the phenyl group, the NNN-based complex could exhibit signs of high selectivity due to its lowest observed binding energies and negative hydride charges. These systems could be examined to determine whether they can contribute to further ligand design.

3.5. Fine-tuning ability

Figures 3.1 and 3.4 show that the nitrogen-based ligands for each substituent exhibit a wider range of binding energies, whereas the phosphorus-based ligands often display comparable energetics in different configurations. This suggests that changes in ligand structures would probably not substantially affect the binding characteristics. In contrast, for nitrogen-based complexes, the variation in functional groups can be used as the tuning gear toward optimizing the affinity of the manganese-based complex toward nitrogen-based heterocycles. However, it does not mean that the intrinsic reactivity of a complex will be as tunable. To examine this, Figure A.12 presents the hydride charges in the molecule on the hydride atom as a function of the reactant and product form of the ligand scaffold and the substitution of the pincer arms. Approximately the exact hydride charges in their product (Pyr-) form are observed for the phosphorus-based and nitrogen-based complexes for all functional groups. This suggests that reactivity is primarily determined by the type of scaffold rather than by the substituent. In general, the reactivity of the hydride and the coordination properties of the ligand can be tuned separately, providing a proper or versatile scope for catalyst design. Together with the electron-donating property of the nitrogen pincer atom, the NNN-based complex and even the NONON-based complex are good candidates for the promotion of tuning of ligand properties, as seen and discussed in the analysis of Figure 3.5.

4

Conclusion and Outlook

4.1. Conclusion

In this thesis, high-throughput screening of manganese-based complexes was conducted to investigate the binding of the substrate, pyridine, to homogeneous hydrogenation. Four pincer ligands (PNP, PONOP, NNN, and NONON) with varying ligand backbones were screened. Each metal-ligand complex accommodates three geometric configurations, with the alignment of the auxiliary carbonyl ligand varying between a hydride (config 1), a pyridine (config 2), and the lutidine part of the nitrogen pincer atom (config 3). To enable successful (de)hydrogenation of pyridine, the stability and reactivity of the complexes were assessed through DFT calculations for each Mn-based complex. The reactivity is also influenced by the design of ligands, since we have investigated how pincer ligands can be designed and which specific substituent can be used to fine-tune the interaction between the metal and the ligand. Hereby, the sensitivity within the backbones of all complexes is taken into account. The variation in pincer ligands and their backbones is key to observing whether a specific complex or configuration is preferred or contributes as a better candidate for fine-tuning. To measure and confirm these aspects, we first analyzed the stability of the complex, focusing on the binding energies of the ligand bound to the substrate ($\Delta G_{\text{reaction}}$). The stability of all complexes could be confirmed if negative $\Delta G_{\text{reaction}}$ values are observed. Unfortunately, all complexes show positive binding energies. The phosphorus-based complexes exhibit steric hindrance, mainly caused by the bulky tert-butyl group, which favors the first configuration. This configuration is unfavorable, as no π-interaction occurs between the auxiliary carbonyl ligand and the hydride atom, which is defined by its σ-donor property. Distortions in the molecular structures of cyclohexane, isopropyl, and methyl are characterized by the bending of the auxiliary ligand, which is caused by the size of the substituent. This leads to unfavorable binding energies and, therefore, unstable complexes. However, there is a preference for the third configuration, as the lowest $\Delta G_{\text{reaction}}$ is observed mainly across all ligand scaffolds and their backbones. This configuration is preferred due to the orbital interaction between the lutidine (π-donor) part of the nitrogen-pincer atom and the auxiliary carbonyl ligand (π-acceptor), which stabilizes the complex. The phenyl substituent in the NNN-based complex is thereby the most promising, providing the lowest Gibbs free energy of the reaction. As the phenyl substituent is characterized by its delocalized π-system, it may contribute to the stability of the complex system. Although the phenyl functional group exhibits stability, the non-existing trend for all complexes does not correlate with the high likelihood of stability for the phenyl substituent. This implies that all complexes occur through outer-sphere mechanisms. The stability of all complexes was further analyzed by observing the binding energy as a function of the bond lengths of the metal with the pyridine. According to the hypothesis, a very low $\Delta G_{\text{reaction}}$ would correlate with a relatively short bond length between the metal and pyridine. The second hypothesis would suggest that strong binding of the metal with pyridine results in the bond length between the metal and the auxiliary carbonyl ligand being relatively long, as this bond faces weak π-backbonding.

However, no clear correlation was observed between the binding energies and the bond lengths of all metal-ligand complexes. The bond lengths are therefore unreliable for forecasting how stable all complexes are.
In terms of the reactivity of all systems, the binding energies were plotted as a function of the distribution of the Mulliken charges on the hydride atom. We consider that higher negative hydride charges correlate with higher reactivity. Only the first configurations exhibit high reactivity in the nitrogen-based complexes for all backbones. The phenyl-substituted system in the nitrogen-based systems illustrates still higher negative hydride charges for the second and third configurations relative to other backbones and the phosphorus-based complex. The hydridic behavior for these complexes could contribute to activating the pyridine-bound complex. However, no correlation is observed between complexes with negative values of $\Delta G_{\text{reaction}}$ and high reactivity, which is our third hypothesis. This further suggests that all complexes operate through outer-sphere mechanisms.
After plotting the binding energies relative to the hydride charge distributions, we observed proper variation in the substituents for the nitrogen-based complexes. The phenyl substituent could be used as a universal design principle for fine-tuning due to its π-π stacking ability and high electron-donating property. Therefore, because this functional group can be further designed to potentially perform inner-sphere mechanisms, ligand design could be encouraged, starting with nitrogen-based complexes. The design of ligands correlates with the reactivity, which is also tunable. This is observed from the plotted hydride charges, which depend only on the type of ligand rather than the substituent, again corresponding to the nitrogen-based complexes. This provides a versatile scope for catalyst design. Thus, with the nitrogen-based complexes, the promising and tunable phenyl-substituent could be used as our base for good ligand design.

4.2. Outlook

This project considered the implications of manganese-based complexes, although a few limitations were also observed. The DFT calculations did not account for solvent interactions. Neither explicit nor implicit solvation models are implemented. Implicit models are recommended because they speed up computations and are therefore less computationally costly [49]. In addition, no correction term of the Gibbs free energy is explicitly considered, for which the entropic cost is relevant. This measurement only considered ideal behavior but does not correspond to the gas phase in which variation in entropy could occur when all reactions are computed. Furthermore, we can benchmark with various functionals such as the hybrid X3LYP functional, which is useful for calculating the hydricity of the hydrogen-bond system [50]. This suggests that the choice of the XC functional influences the electronic properties, which determine the activity and reactivity of the metal complexes. As concluded from this thesis, the phenyl group exhibits the lowest binding energies and could be proposed as a good starting point for improving the stability of the complex. Further research should support the screening of pincer ligand complexes using phenyl-based backbones. A recent study used this approach for the hydrogenation of indanone to improve enantioselectivity, for which phenyl-related substituents could be added to pincer-bound ligands that increase the π-system [51]. Together with this non-covalent interaction, the larger delocalized system causes the metal complex to be more stabilized[51]. In our case, when pyridine binds to the complex, this could improve the π-π stacking phenomenon. Thereby, transition states from the NNP-complex could improve the enantioselectivity by applying steric bulk around the active site of the complex [51]. Here, the added steric group could force the substrate to position from the northern hemisphere to the southern hemisphere of the complex, as seen in figure A.13[51]. A greater volume difference between the two environments indicates high selectivity and a more favorable transition state for, in our case, pyridine to bind to the complex [51]. However, the sterically hindered group may not be able to bind to the metal. In our case, the design could still be improved due to the non-electron-withdrawing property of the fully nitrogen-based complexes, as opposed to the NNP-metal ligand complex used in the study.
Three various hypotheses were adopted to explain our results, but should be examined more in detail. The first two hypotheses discuss the increase in binding energy that would correlate to the rise in the bond length between the metal and pyridine. Secondly, a relatively long metal-pyridine bond length could correspond to a relatively short metal-auxiliary carbonyl bond due to strong π-back bonding. As these bond lengths were not representative, it is considered to focus on other electronic descriptors, such as the vibrating frequency

analysis of the CO bond, to study these parameters more in detail [26]. Thirdly, in terms of reactivity, a more negative hydride charge would indicate higher reactivity. To confirm this hypothesis, the reaction kinetics and energy barriers of (de)hydrogenation of pyridine should be fully taken into account.
A few assumptions were also made, which should be further studied to test its reliability. The electronic compensation of the pyridine and auxiliary carbonyl ligand bonds to the metal, affected the $\Delta G_{\text{reaction}}$ of the tert-butyl group by lowering this value compared to the small methyl group. This observation should be further investigated by implementing additional descriptors to quantify the role of electronic compensation in the presence of bulky groups across other ligand scaffolds. Such electronic descriptors include the ionization potential, which examines the reactivity of the complex by computing the energy between the molecule and the cation [52]. We could further investigate this compensation as the ORCA software enables us to analyze the natural bond orbital (NBO). This method further studies the interactions between the intra- and intermolecular bonds within the metal ligand complex [53]. We also assume that all metal-ligand complexes perform outer-sphere mechanisms. The negative Mulliken charges encourage this, as the nitrogen pincer arm binds weakly compared to that of the phosphorus atoms. This is relevant as the reactivity of the complex could be further explored.
It would be relevant to focus on the displacement of the pincer arms, such as the nitrogen and phosphorus arms, to examine the hemilability of the complex. An earlier attempt was made to examine the hemilabile nature of two Mn-based NNP-pincer ligand complexes that vary only in bridge length [54]. Unfortunately, no signs of temporary unbinding of the phosphine pincer ligands could be observed due to the high decoordination energy of both complexes relative to the activation of hydrogen atoms in the complex [54]. This indicates that for our metal complex structures, hemilability is likely to occur as no stable structures are observed.

Bibliography

[1] Suresh Kumar, Gourav Kumar, Bhavna Saroha, and Kapil Gulati. 12 - Metal oxide heterostructures as catalysts in organic reactions. In Naveen Kumar, Bernabé Marí Soucase, and Ghenadii Korotcenkov, editors, *Metal Oxide-Based Heterostructures*, Metal Oxides, pages 417–451. Elsevier, January 2023. ISBN 978-0-323-85241-8. doi: 10.1016/B978-0-323-85241-8.00003-7. URL https://www.sciencedirect.com/science/article/pii/B9780323852418000037.

[2] Matthew G. Quesne, Fabrizio Silveri, Nora H. de Leeuw, and C. Richard A. Catlow. Advances in Sustainable Catalysis: A Computational Perspective. *Frontiers in Chemistry*, 7, April 2019. ISSN 2296-2646. doi: 10.3389/fchem.2019.00182. URL https://www.frontiersin.orghttps://www.frontiersin.org/journals/chemistry/articles/10.3389/fchem.2019.00182/full.

[3] Batoul Taleb, Rabih Jahjah, David Cornu, Mikhael Bechelany, Mohamad Al Ajami, Ghenwa Kataya, Akram Hijazi, and Mohammad H. El-Dakdouki. Exploring Hydrogen Sources in Catalytic Transfer Hydrogenation: A Review of Unsaturated Compound Reduction. *Molecules*, 28(22):7541, November 2023. ISSN 1420-3049. doi: 10.3390/molecules28227541. URL https://www.ncbi.nlm.nih.gov/pmc/articles/PMC10673347/.

[4] Lucía Morán-González, Arron L. Burnage, Ainara Nova, and David Balcells. AI Approaches to Homogeneous Catalysis with Transition Metal Complexes. *ACS Catalysis*, 15(11):9089–9105, June 2025. doi: 10.1021/acscatal.5c01202. URL https://doi.org/10.1021/acscatal.5c01202.

[5] Renyang Zheng, Zhicheng Liu, Yangdong Wang, Zaiku Xie, and Mingyuan He. The future of green energy and chemicals: Rational design of catalysis routes. *Joule*, 6(6):1148–1159, June 2022. ISSN 2542-4351. doi: 10.1016/j.joule.2022.04.014. URL https://www.sciencedirect.com/science/article/pii/S2542435122001817.

[6] Zhihui Shao, Yang Li, Chenguang Liu, Wenying Ai, Shu-Ping Luo, and Qiang Liu. Reversible interconversion between methanol-diamine and diamide for hydrogen storage based on manganese catalyzed (de)hydrogenation. *Nature Communications*, 11(1):591, January 2020. ISSN 2041-1723. doi: 10.1038/s41467-020-14380-3. URL https://www.nature.com/articles/s41467-020-14380-3.

[7] Abdisa Sisay Mekonnin, Krzysztof Wacławiak, Muhammad Humayun, Shaowei Zhang, and Habib Ullah. Hydrogen Storage Technology, and Its Challenges: A Review. *Catalysts*, 15(3):260, March 2025. ISSN 2073-4344. doi: 10.3390/catal15030260. URL https://www.mdpi.com/2073-4344/15/3/260.

[8] Amit Kumar, Prosenjit Daw, and David Milstein. Homogeneous Catalysis for Sustainable Energy: Hydrogen and Methanol Economies, Fuels from Biomass, and Related Topics. *Chemical Reviews*, 122(1):385–441, January 2022. ISSN 0009-2665. doi: 10.1021/acs.chemrev.1c00412. URL https://doi.org/10.1021/acs.chemrev.1c00412.

[9] Huda S. Alghamdi, Ahsan Ali, Afnan M. Ajeebi, Abdesslem Jedidi, Mohammed Sanhoob, Mahbuba Aktary, A. H. Shabi, Mohammad Usman, Wasan Alghamdi, Shahad Alzahrani, Md. Abdul Aziz, and M. Nasiruzzaman Shaikh. Catalysts for Liquid Organic Hydrogen Carriers (LOHCs): Efficient Storage and Transport for Renewable Energy. *The Chemical Record*, 24(11):e202400082, 2024. ISSN 1528-0691. doi: 10.1002/tcr.202400082. URL https://onlinelibrary.wiley.com/doi/abs/10.1002/tcr.202400082.

[10] Min-Jie Zhou, Yulong Miao, Yanwei Gu, and Yinjun Xie. Recent Advances in Reversible Liquid Organic Hydrogen Carrier Systems: From Hydrogen Carriers to Catalysts. *Advanced Materials*, 36(37):2311355, 2024. ISSN 1521-4095. doi: 10.1002/adma.202311355. URL https://onlinelibrary.wiley.com/doi/abs/10.1002/adma.202311355.

[11] Jinho Oh, Kwanyong Jeong, Tae Wan Kim, Hyunguk Kwon, Jeong Woo Han, Ji Hoon Park, and Young-Woong Suh. 2-(N-Methylbenzyl)pyridine: A Potential Liquid Organic Hydrogen Carrier with Fast H2 Release and Stable Activity in Consecutive Cycles. *ChemSusChem*, 11(4):661–665, February 2018. ISSN 1864-5631. doi: 10.1002/cssc.201702256. URL https://chemistry.europe.onlinelibrary.wiley.com/doi/full/10.1002/cssc.201702256.

[12] M. Niermann, S. Timmerberg, S. Drünert, and M. Kaltschmitt. Liquid Organic Hydrogen Carriers and alternatives for international transport of renewable hydrogen. *Renewable and Sustainable Energy Reviews*, 135:110171, January 2021. ISSN 1364-0321. doi: 10.1016/j.rser.2020.110171. URL https://www.sciencedirect.com/science/article/pii/S1364032120304627.

[13] Georgy A. Filonenko, Robbert van Putten, Emiel J. M. Hensen, and Evgeny A. Pidko. Catalytic (de)hydrogenation promoted by non-precious metals – Co, Fe and Mn: recent advances in an emerging field. *Chemical Society Reviews*, 47(4):1459–1483, February 2018. ISSN 1460-4744. doi: 10.1039/C7CS00334J. URL https://pubs.rsc.org/en/content/articlelanding/2018/cs/c7cs00334j.

[14] Andy Lin and Giuseppe Bagnato. Revolutionising energy storage: The Latest Breakthrough in liquid organic hydrogen carriers. *International Journal of Hydrogen Energy*, 63:315–329, April 2024. ISSN 0360-3199. doi: 10.1016/j.ijhydene.2024.03.146. URL https://www.sciencedirect.com/science/article/pii/S0360319924009789.

[15] Robert H. Crabtree. Nitrogen-Containing Liquid Organic Hydrogen Carriers: Progress and Prospects. *ACS Sustainable Chemistry & Engineering*, 5(6):4491–4498, June 2017. doi: 10.1021/acssuschemeng.7b00983. URL https://doi.org/10.1021/acssuschemeng.7b00983.

[16] Viktoriia Zubar, Jannik C. Borghs, and Magnus Rueping. Hydrogenation or Dehydrogenation of N-Containing Heterocycles Catalyzed by a Single Manganese Complex. *Organic Letters*, 22(10):3974–3978, May 2020. ISSN 1523-7060. doi: 10.1021/acs.orglett.0c01273. URL https://doi.org/10.1021/acs.orglett.0c01273.

[17] Pyridine Ligands - Catalysts / Alfa Chemistry, . URL https://www.alfachemic.com/catalysts/products/pyridine-ligands.html.

[18] Yujie Wang, Mingyang Wang, Yibiao Li, and Qiang Liu. Homogeneous manganese-catalyzed hydrogenation and dehydrogenation reactions. *Chem*, 7(5):1180–1223, May 2021. ISSN 2451-9294. doi: 10.1016/j.chempr.2020.11.013. URL https://www.sciencedirect.com/science/article/pii/S2451929420305969.

[19] Kuhali Das, Satyadeep Waiba, Akash Jana, and Biplab Maji. Manganese-catalyzed hydrogenation, dehydrogenation, and hydroelementation reactions. *Chemical Society Reviews*, 51(11):4386–4464, June 2022. ISSN 1460-4744. doi: 10.1039/D2CS00093H. URL https://pubs.rsc.org/en/content/articlelanding/2022/cs/d2cs00093h.

[20] Eduardo Peris and Robert H. Crabtree. Key factors in pincer ligand design. *Chemical Society Reviews*, 47(6):1959–1968, March 2018. ISSN 1460-4744. doi: 10.1039/C7CS00693D. URL https://pubs.rsc.org/en/content/articlelanding/2018/cs/c7cs00693d.

[21] Eric S. Wiedner, Matthew B. Chambers, Catherine L. Pitman, R. Morris Bullock, Alexander J. M. Miller, and Aaron M. Appel. Thermodynamic Hydricity of Transition Metal Hydrides. *Chemical Reviews*, 116(15):8655–8692, August 2016. ISSN 0009-2665. doi: 10.1021/acs.chemrev.6b00168. URL https://doi.org/10.1021/acs.chemrev.6b00168.

[22] Chenguang Liu, Mingyang Wang, Shihan Liu, Yujie Wang, Yong Peng, Yu Lan, and Qiang Liu. Manganese-Catalyzed Asymmetric Hydrogenation of Quinolines Enabled by – Interaction. *Angewandte Chemie International Edition*, 60(10):5108–5113, 2021. ISSN 1521-3773. doi: 10.1002/anie.202013540. URL https://onlinelibrary.wiley.com/doi/abs/10.1002/anie.202013540.

[23] Arthur Despois and Nicolai Cramer. Iridium(III)-Catalyzed Ionic Hydrogenation of Pyridines to Multi-Substituted Piperidines, April 2025. URL https://chemrxiv.org/engage/chemrxiv/article-details/680f3cfa50018ac7c58462dc.

[24] Biplab Maji and Milan K. Barman. Recent Developments of Manganese Complexes for Catalytic Hydrogenation and Dehydrogenation Reactions. *Synthesis*, 49:3377–3393, July 2017. ISSN 0039-7881. doi: 10.1055/s-0036-1590818. URL https://www.thieme.connect.com/products/ejournals/abstract/10.1055/s-0036-1590818.

[25] Dennis Verspeek, Sebastian Ahrens, Anke Spannenberg, Xiaodong Wen, Yong Yang, Yong-Wang Li, Kathrin Junge, and Matthias Beller. Manganese N,N,N-pincer complex-catalyzed epoxidation of unactivated aliphatic olefins. *Catalysis Science & Technology*, 12(24):7341–7348, December 2022. ISSN 2044-4761. doi: 10.1039/D2CY01472F. URL https://pubs.rsc.org/en/content/articlelanding/2022/cy/d2cy01472f.

[26] Yujie Wang, Lei Zhu, Zhihui Shao, Gang Li, Yu Lan, and Qiang Liu. Unmasking the Ligand Effect in Manganese-Catalyzed Hydrogenation: Mechanistic Insight and Catalytic Application. *Journal of the American Chemical Society*, 141(43):17337–17349, October 2019. ISSN 0002-7863. doi: 10.1021/jacs.9b09038. URL https://doi.org/10.1021/jacs.9b09038.

[27] Emma J. Jordan, Ethan D. E. Calder, Bethan L. Greene, Holly V. Adcock, Louise Male, Paul W. Davies, and Andrew R. Jupp. Tuning the Electronic Properties of Azophosphines as Ligands and Their Application in Base-Free Transfer Hydrogenation Catalysis. *Organometallics*, 43(20):2674–2685, October 2024. ISSN 0276-7333. doi: 10.1021/acs.organomet.4c00302. URL https://doi.org/10.1021/acs.organomet.4c00302.

[28] Adarsh V. Kalikadien, Adrian Mirza, Aydin Najl Hossaini, Avadakkam Sreenithya, and Evgeny A. Pidko. Paving the road towards automated homogeneous catalyst design. *ChemPlusChem*, 89(7):e202300702, July 2024. ISSN 2192-6506. doi: 10.1002/cplu.202300702. URL https://chemistry.europe.onlinelibrary.wiley.com/doi/10.1002/cplu.202300702.

[29] Aditya Nandy, Chenru Duan, Michael G. Taylor, Fang Liu, Adam H. Steeves, and Heather J. Kulik. Computational Discovery of Transition-metal Complexes: From High-throughput Screening to Machine Learning. *Chemical Reviews*, 121(16):9927–10000, August 2021. ISSN 0009-2665. doi: 10.1021/acs.chemrev.1c00347. URL https://doi.org/10.1021/acs.chemrev.1c00347.

[30] Ivan Yu. Chernyshov and Evgeny A. Pidko. MACE: Automated Assessment of Stereochemistry of Transition Metal Complexes and Its Applications in Computational Catalysis. *Journal of Chemical Theory and Computation*, 20(5):2313–2320, March 2024. ISSN 1549-9618. doi: 10.1021/acs.jctc.3c01313. URL https://doi.org/10.1021/acs.jctc.3c01313.

[31] Marvin - Chemical Drawing Software, . URL https://chemaxon.com/marvin.

[32] The Avogadro Team. Avogadro - Free cross-platform molecular editor, January 2022. URL https://avogadro.cc/.

[33] N Y Acelas and E Flórez. Density functional theory studies of the adsorption of Cr (VI) on Fe-(hydr) oxide: Gibbs free energies and pH effect. *Journal of Physics: Conference Series*, 1247(1):012051, June 2019. ISSN 1742-6596. doi: 10.1088/1742-6596/1247/1/012051. URL https://dx.doi.org/10.1088/1742-6596/1247/1/012051.

[34] Jordan Labrecque, Yae-In Cho, Daniel K. McIntosh, Faridat Agboola, and Michael J. Rose. Distal scaffold flexibility accelerates ligand substitution kinetics in manganese(I) tricarbonyls: flexible thianthrene versus rigid anthracene scaffolds. *Dalton Transactions*, 52(13):4028–4037, March 2023. ISSN 1477-9234. doi: 10.1039/D2DT04048D. URL https://pubs.rsc.org/en/content/articlelanding/2023/dt/d2dt04048d.

[35] Frank Neese, Frank Wennmohs, Ute Becker, and Christoph Riplinger. The ORCA quantum chemistry program package. *The Journal of Chemical Physics*, 152(22):224108, June 2020. ISSN 0021-9606. doi: 10.1063/5.0004608. URL https://doi.org/10.1063/5.0004608.

[36] Daniel Fritsch, Benjamin J. Morgan, and Aron Walsh. Self-Consistent Hybrid Functional Calculations: Implications for Structural, Electronic, and Optical Properties of Oxide Semiconductors. *Nanoscale Research Letters*, 12(1):1–7, December 2017. ISSN 1556-276X. doi: 10.1186/s11671-016-1779-9. URL https://link-springer-com.tudelft.idm.oclc.org/article/10.1186/s11671-016-1779-9.

[37] José A. Gámez, Markus Hölscher, and Walter Leitner. On the applicability of density functional theory to manganese-based complexes with catalytic activity toward water oxidation. *Journal of Computational Chemistry*, 38(20):1747–1751, 2017. ISSN 1096-987X. doi: 10.1002/jcc.24819. URL https://onlinelibrary.wiley.com/doi/abs/10.1002/jcc.24819.

[38] Stefan Grimme, Stephan Ehrlich, and Lars Goerigk. Effect of the damping function in dispersion corrected density functional theory. *Journal of Computational Chemistry*, 32(7):1456–1465, 2011. ISSN 1096-987X. doi: 10.1002/jcc.21759. URL https://onlinelibrary.wiley.com/doi/abs/10.1002/jcc.21759.

[39] Mauricio Cafiero. Role of Exact Exchange and Empirical Dispersion in Density Functional Theory-Based Three-Body Noncovalent Interactions. *The Journal of Physical Chemistry A*, 128(40):8777–8786, October 2024. ISSN 1089-5639. doi: 10.1021/acs.jpca.4c03262. URL https://doi.org/10.1021/acs.jpca.4c03262.

[40] Florian Weigend and Reinhart Ahlrichs. Balanced basis sets of split valence, triple zeta valence and quadruple zeta valence quality for H to Rn: Design and assessment of accuracy. *Physical Chemistry Chemical Physics*, 7(18):3297–3305, 2005. doi: 10.1039/B508541A. URL https://pubs.rsc.org/en/content/articlelanding/2005/cp/b508541a.

[41] Ramin Miri, Nima Razzaghi-asl, and Mohammad K. Mohammadi. QM study and conformational analysis of an isatin Schiff base as a potential cytotoxic agent. *Journal of Molecular Modeling*, 19(2):727–735, February 2013. ISSN 0948-5023. doi: 10.1007/s00894-012-1586-x. URL https://doi.org/10.1007/s00894-012-1586-x.

[42] Ioanna Pallikara, Prakriti Kayastha, Jonathan M Skelton, and Lucy D Whalley. The physical significance of imaginary phonon modes in crystals. *Electronic Structure*, 4(3):033002, July 2022. ISSN 2516-1075. doi: 10.1088/2516-1075/ac78b3. URL https://dx.doi.org/10.1088/2516-1075/ac78b3.

[43] G. In Cutler J. Cleveland and Christopher Morris, editors, *Dictionary of Energy (Second Edition)*, pages 247–273. Elsevier, Boston, January 2015. ISBN 9780080968117. doi: 10.1016/B978-0-08-096811-7.50007-X. URL https://www.sciencedirect.com/science/article/pii/B978008096811750007X.

[44] Bin Wan, Marta Castiñeira Reis, Tizian-Frank Ramspoth, and Syuzanna R. Harutyunyan. Manganese(I)-Catalyzed Enantioselective Alkylation To Access P-Stereogenic Phosphines. *Journal of the American Chemical Society*, 147(4):3740–3746, January 2025. ISSN 0002-7863. doi: 10.1021/jacs.4c16130. URL https://doi.org/10.1021/jacs.4c16130.

[45] Boltzmann weight - Encyclopedia of Mathematics, . URL https://encyclopediaofmath.org/wiki/Boltzmann_weight.

[46] Saurabh Vinod Parmar, Vidya Avasare, and Sourav Pal. Unraveling the Effect of Aromatic Groups in Mn(I)NNN Pincer Complexes on Carbon Dioxide Activation Using Density Functional Study. *Frontiers in Chemistry*, 9, November 2021. ISSN 2296-2646. doi: 10.3389/fchem.2021.778718. URL https://www.frontiersin.org/journals/chemistry/articles/10.3389/fchem.2021.778718/full.

[47] Matheus S. S. Paqui, Vinícius A. Glitz, Daniele C. Durigon, André L. Amorim, Giovanni F. Caramori, Renato L. T. Parreira, Adailton J. Bortoluzzi, Fernando R. Xavier, and Rosely A. Peralta. Spectroscopical and Molecular Studies of Four Manganese(I) PhotoCORMs with Bioinspired Ligands Containing Non-Coordinated Phenol Groups. *Molecules*, 28(8):3439, January 2023. ISSN 1420-3049. doi: 10.3390/molecules28083439. URL https://www.mdpi.com/1420-3049/28/8/3439.

[48] Giovanni Bistoni, Sergio Rampino, Nicola Scafuri, Gianluca Ciancaleoni, Daniele Zuccaccia, Leonardo Belpassi, and Francesco Tarantelli. How back-donation quantitatively controls the CO stretching response in classical and non-classical metal carbonyl complexes. *Chemical Science*, 7(2):1174–1184, January 2016. ISSN 2041-6539. doi: 10.1039/C5SC02971F. URL https://pubs.rsc.org/en/content/articlelanding/2016/sc/c5sc02971f.

[49] Péter Pál Fehér and András Stirling. Assessment of reactivities with explicit and implicit solvent models: QM/MM and gas-phase evaluation of three different Ag-catalysed furan ring formation routes. *New Journal of Chemistry*, 43(39):15706–15713, 2019. doi: 10.1039/C9NJ04003J. URL https://pubs.rsc.org/en/content/articlelanding/2019/nj/c9nj04003j.

[50] Biswajit Santra, Angelos Michaelides, and Matthias Scheffler. On the accuracy of density-functional theory exchange-correlation functionals for H bonds in small water clusters: Benchmarks approaching the complete basis set limit. *The Journal of Chemical Physics*, 127(18), November 2007. ISSN 0021-9606. doi: 10.1063/1.2790009. URL https://pubs.aip.org/aip/jcp/article/127/18/184104/928411/On-the-accuracy-of-density-functional-theory.

[51] Alister S. Goodfellow, Matthew L. Clarke, and Michael Bühl. Computational Exploration of Stereoelectronic Relationships in Manganese-Catalyzed Hydrogenation Reactions. *Chemistry (Weinheim an Der Bergstrasse, Germany)*, 31(34):e202501063, June 2025. ISSN 0947-6539. doi: 10.1002/chem.202501063. URL https://www.ncbi.nlm.nih.gov/pmc/articles/PMC12172583/.

[52] J. S. Shang. Recent research in magneto-aerodynamics. *Progress in Aerospace Sciences*, 37(1):1–20, January 2001. ISSN 0376-0421. doi: 10.1016/S0376-0421(00)00015-4. URL https://www.sciencedirect.com/science/article/pii/S0376042100000154.

[53] Lafifi Ismahan, Nouar Leila, Madi Fatiha, Guendouzi Abdelkrim, Cheriet Mouna, Boulaha Nada, and Houari Brahim. Computational study of inclusion complex of l-Glutamine/beta-Cycldextrin: Electronic and intermolecular interactions investigations. *Journal of Molecular Structure*, 1206:127740, April 2020. ISSN 0022-2860. doi: 10.1016/j.molstruc.2020.127740. URL https://www.sciencedirect.com/science/article/pii/S0022286020300648.

[54] Veronica Papa, Johannes Fessler, Francesco Zaccaria, Julien Hervochon, Phong Dam, Christoph Kubis, Anke Spannenberg, Zhihong Wei, Haijun Jiao, Cristiano Zuccaccia, Alceo Macchioni, Kathrin Junge, and Matthias Beller. Efficient Hydrogenation of N-Heterocycles Catalyzed by NNP–Manganese(I) Pincer Complexes at Ambient Temperature. *Chemistry – A European Journal*, 29(2):e202202774, January 2023. ISSN 0947-6539. doi: 10.1002/chem.202202774. URL https://chemistry-europe-onlinelibrary-wiley-com.tudelft.idm.oclc.org/doi/full/10.1002/chem.202202774.

A

Extra figures

Table A.1: Stefan Bolztmann weight of configuration distribution (%) across different backbones and substituents

Backbone	**Substituent**	**Order**	**Configuration 1 (%)**	**Configuration 2 (%)**	**Configuration 3 (%)**
PNP	Cy	1	0.000	0.001	99.999
PNP	Me	2	92.421	0.000	7.579
PNP	Ph	3	0.297	0.000	99.703
PNP	iPr	4	47.900	0.000	52.100
PNP	tBu	5	0.019	0.001	99.979
PONOP	Cy	1	99.114	0.000	0.886
PONOP	Me	2	49.754	0.028	50.218
PONOP	Ph	3	51.010	0.001	48.989
PONOP	iPr	4	0.095	0.000	99.905
PONOP	tBu	5	50.443	0.001	49.556
NNN	Cy	1	0.000	87.907	12.093
NNN	Me	2	50.638	0.000	49.362
NNN	Ph	3	48.669	2.661	48.669
NNN	iPr	4	99.800	0.000	0.200
NNN	tBu	5	1.055	5.600	93.345
NONON	Cy	1	49.904	50.096	0.000
NONON	Me	2	50.156	0.000	49.844
NONON	Ph	3	53.794	0.007	46.199
NONON	iPr	4	50.051	0.334	49.615
NONON	tBu	5	22.885	60.021	17.094

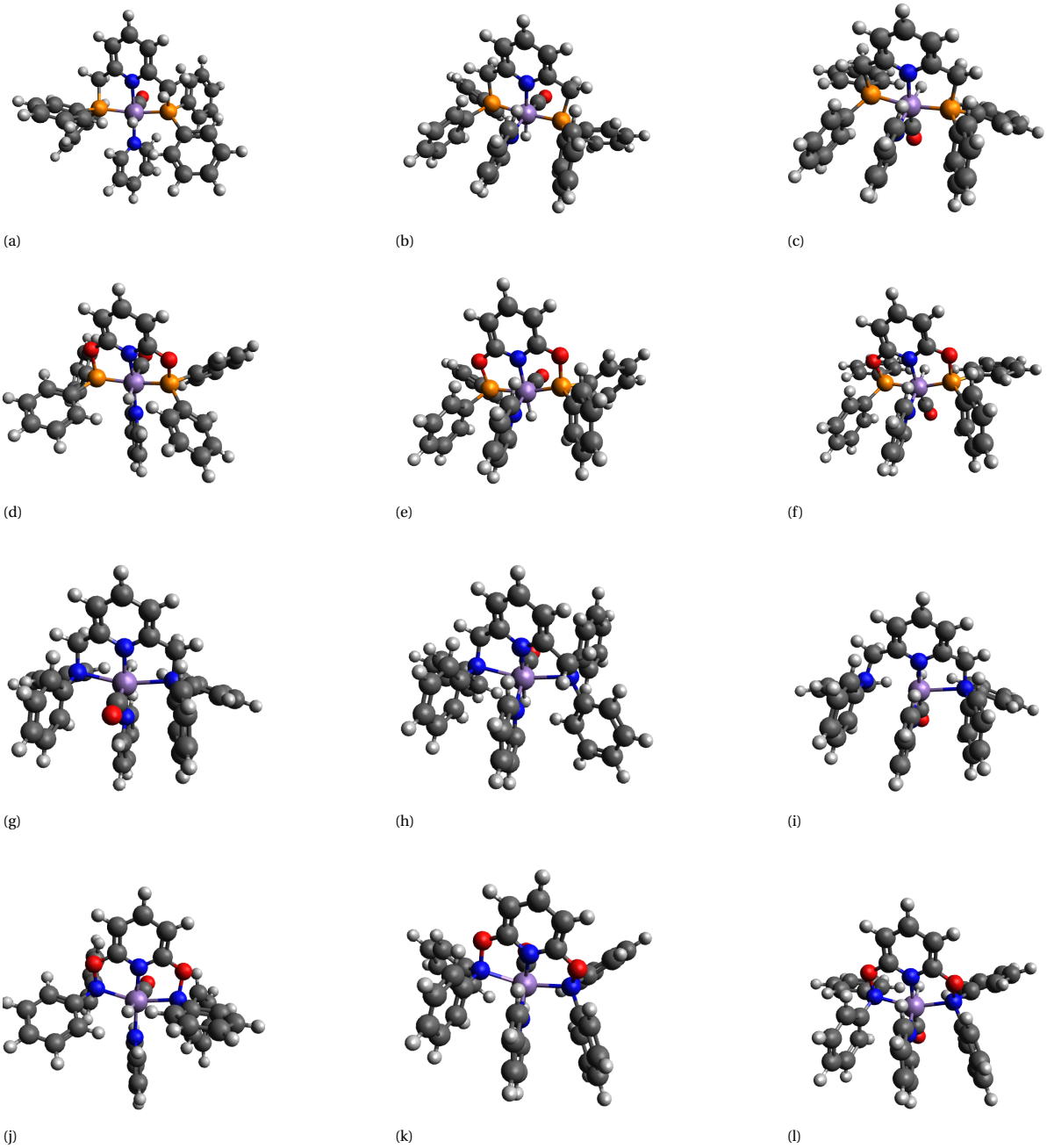

(a) (b) (c)

(d) (e) (f)

(g) (h) (i)

(j) (k) (l)

Figure A.1: The three geometries of L_3MnH(CO)$_2$ for phenyl as substituent for PNP (a-c), PONOP (d-f), NNN (g-i) and NONON (j-l)ligand types for illustrating the preferred alignment of pyridine through π-π stacking

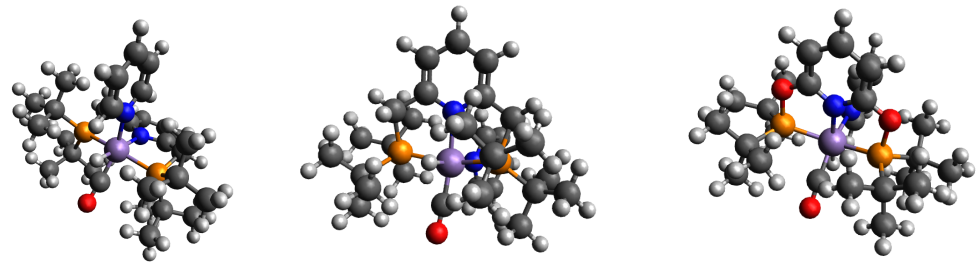

(a) (b) (c)

Figure A.2: Unfavorable coordination of Mn-based complex structure with bulky tert-butyl substituent due to bending of auxiliary CO ligand observed for PNP-configuration 2 (a) PNP-configuration 3 (b) and PONOP-configuration 2 (c)

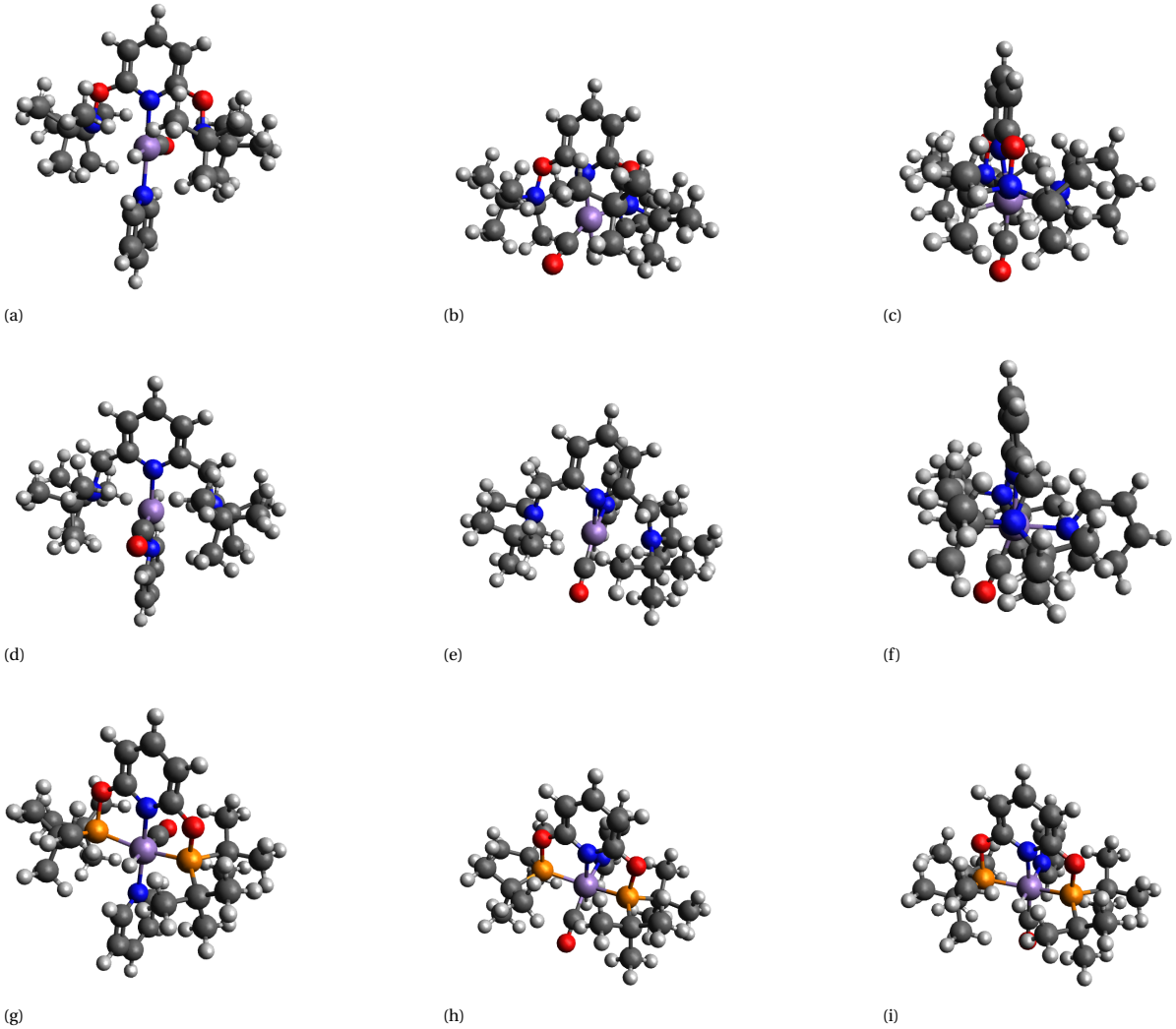

(a) (b) (c)

(d) (e) (f)

(g) (h) (i)

Figure A.3: The three geometries of L_3MnH(CO)$_2$ for side-coordinated tert-butyl as substituent for NONON (a-c), NNN (d-f) and PONOP (g-i) ligand types

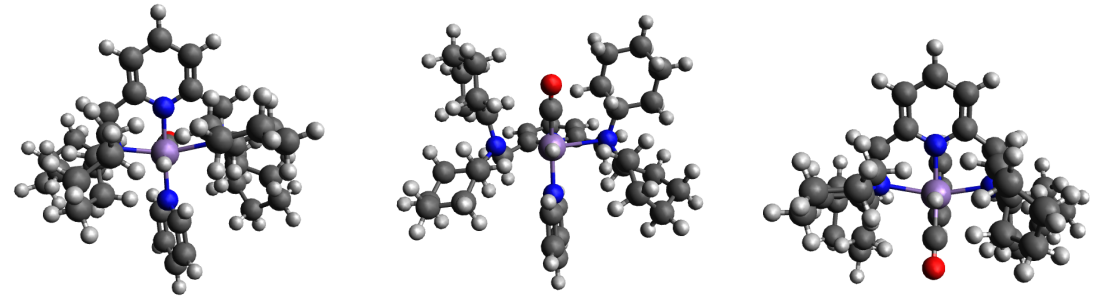

(a) (b) (c)

Figure A.4: The large environment of cyclohexane potentially causing hindrance of the hydride atom within the NNN-based complex; configuration 1 (a) configuration 2 (b) and configuration (3)

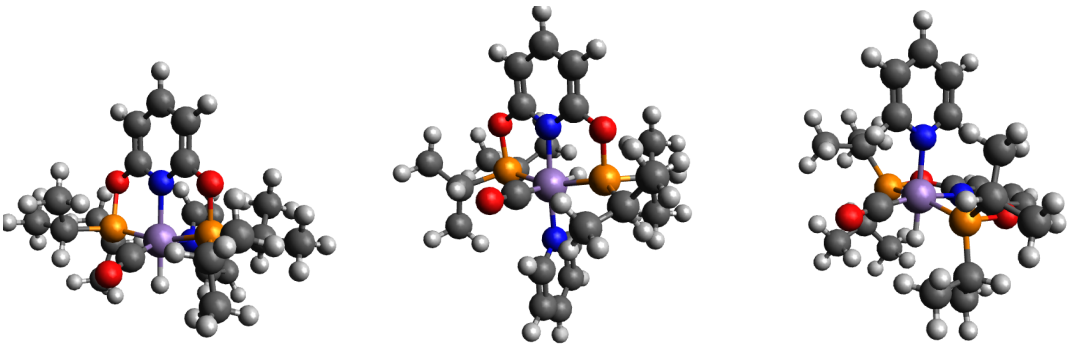

(a) (b) (c)

Figure A.5: Unfavorable coordination of Mn-based complex structure with large isopropyl substituent due to bending of auxiliary CO ligand observed mainly for PONOP-configuration 2 (a) rather than PONOP-configuration 1 (b) and PONOP-configuration 3 (c)

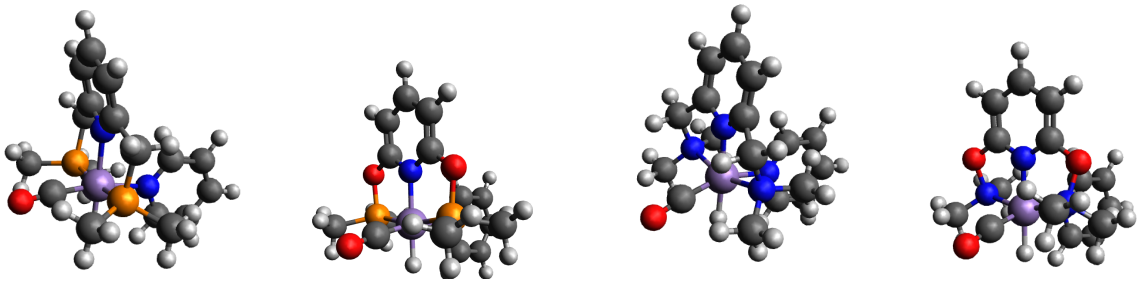

(a) (b) (c) (d)

Figure A.6: Unfavorable coordination of complex structure with the small methyl functional group for the second configurations across all ligand types; PNP (a), PONOP (b), NNN (c) and NONON (d)

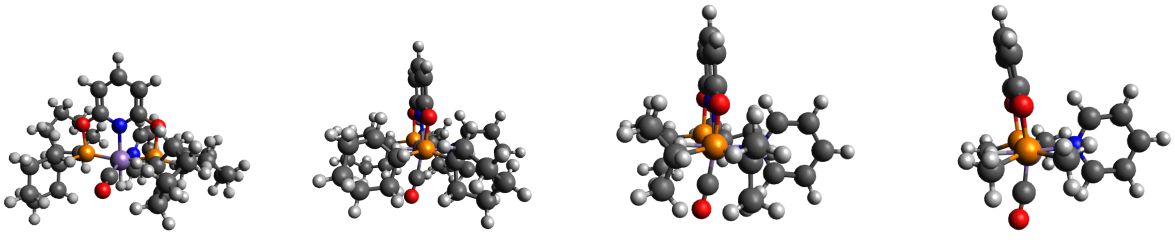

(a) (b) (c) (d)

Figure A.7: Unfavorable coordination of complex structure with the cyclohexane, isopropyl and methyl substituents illustrating CO bending for second and mainly third configurations of PONOP ligand scaffold; PONOP-Cy configuration 2, highest $\Delta G_{\text{reaction}}$ (a), PONOP-Cy configuration 3 (b), PONOP-iPr configuration 3 (c) and PONOP-Me configuration 3 (d)

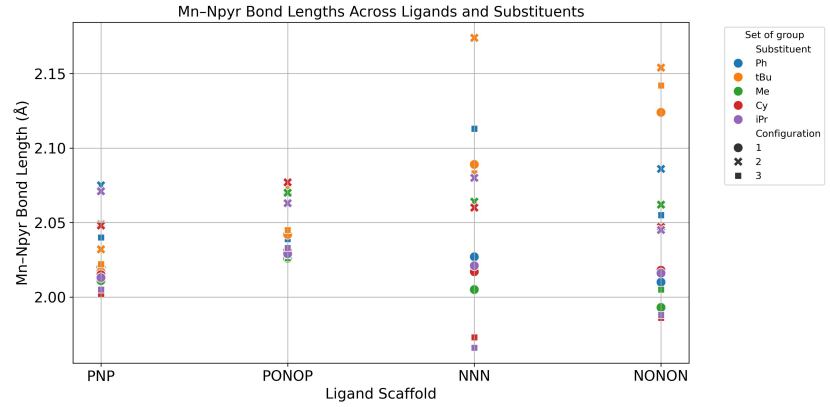

(a)

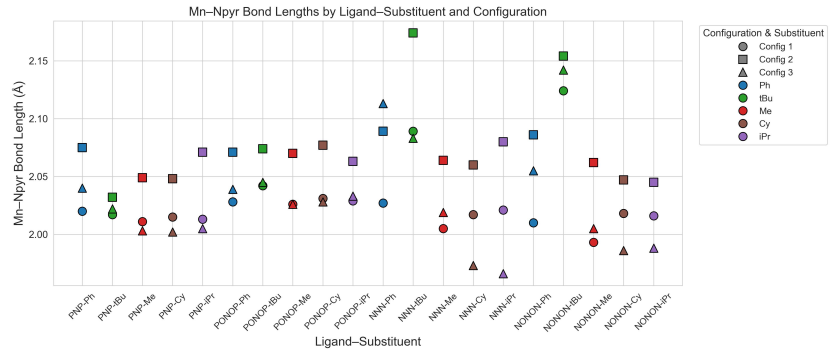

(b)

Figure A.8: Metal-pyridine bond length as function of the ligand type, substituent, and configurations in two various forms. (a) Catplot of the distribution of the metal-pyr bond length plotted against each ligand type, with configurations(b) Scatterplot of the distribution of the metal-pyr bond length plotted against each ligand-substituent, defining the configurations.

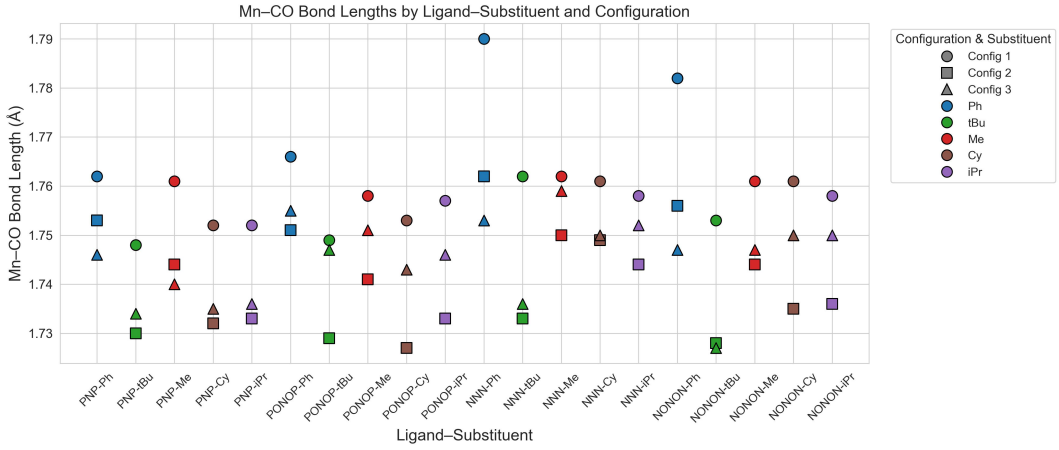

Figure A.9: Scatterplot of the distribution of the metal-CO bond length plotted against each ligand-substituent, defining the configurations

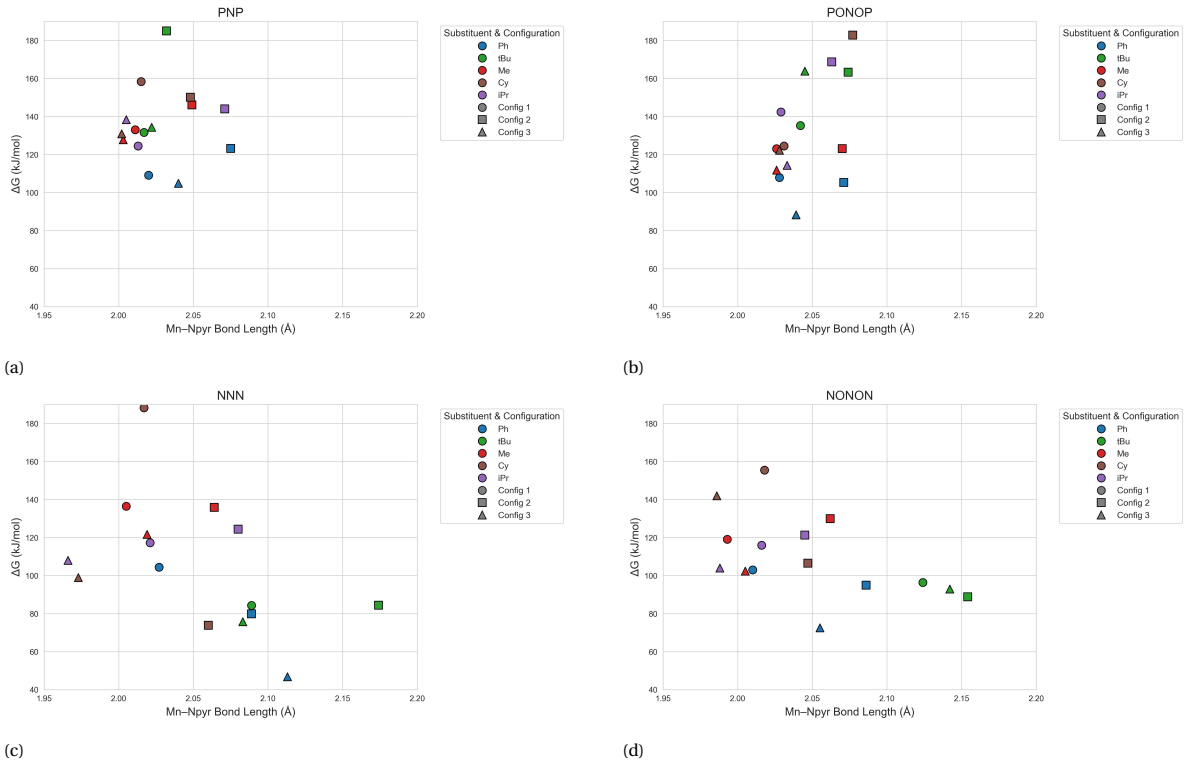

Figure A.10: Gibbs free energy of reaction ($\Delta G_{\text{reaction}}$) plotted against the hydride charge distribution with the focus on each ligand types and their configurations; PNP (a), PONOP (b), NNN (c) and NONON (d)

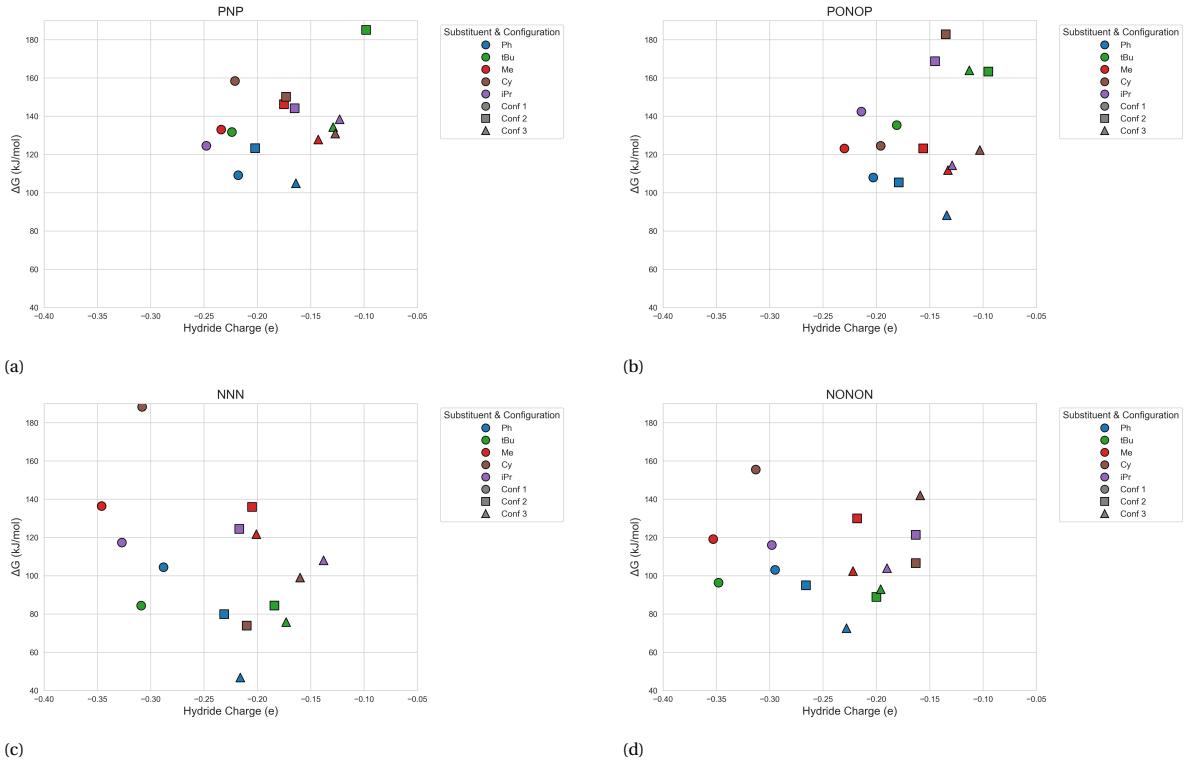

Figure A.11: Gibbs free energy of reaction ($\Delta G_{\text{reaction}}$) against the hydride charge distribution with the focus on each ligand types and their configurations; PNP (a), PONOP (b), NNN (c) and NONON (d)

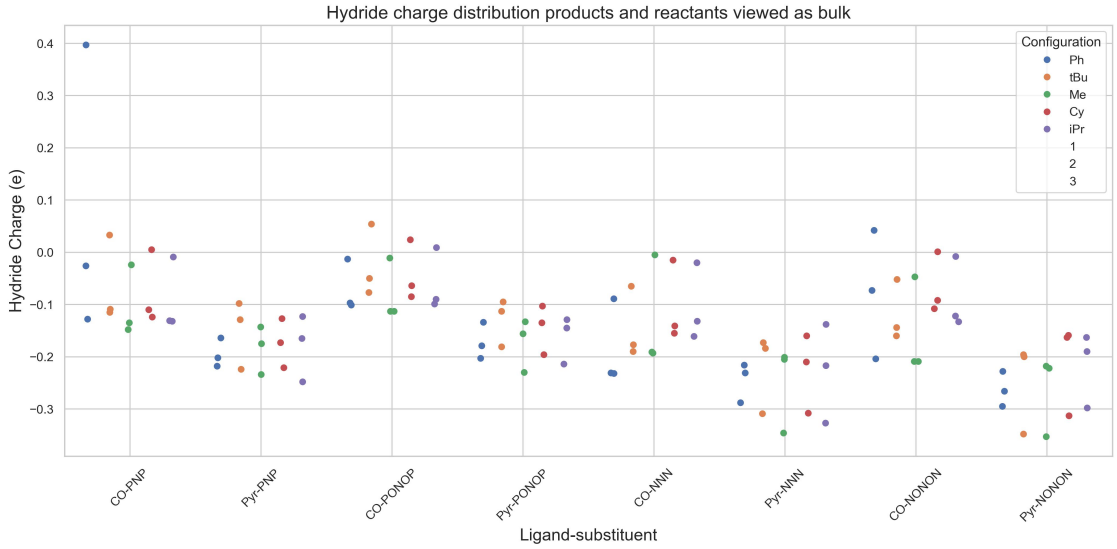

Figure A.12: Hydride charge distribution of each ligand-substituent based on the reactant (CO-) complex and product (Pyr-) complex

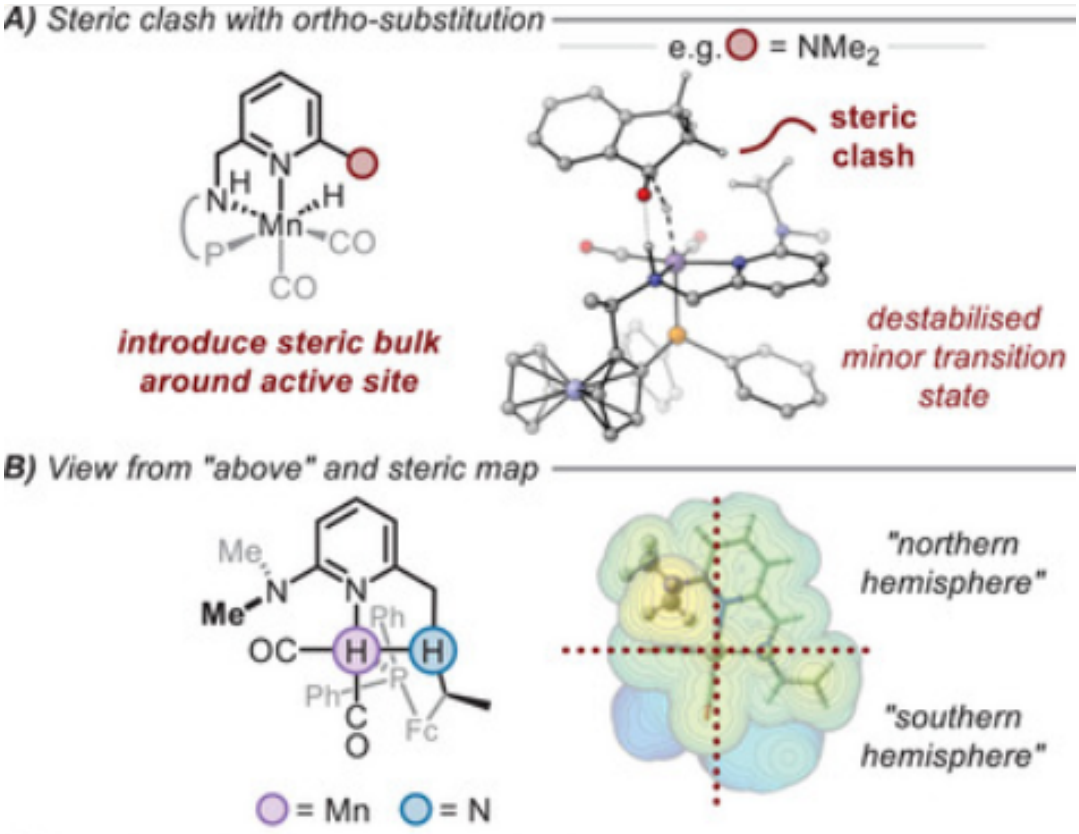

Figure A.13: An Attempt for ligand design by implementing steric bulk near the active site[51]

B

AI statement

The use of ChatGPT was limited to improving understanding of theoretical aspects, ensuring correct language use, and improving efficiency in literature research. In addition, calculations with Python were enhanced and refined through the use of AI. This also accounts for the Boltzmann distribution formula (Section 3.2), which required additional support to integrate into the LaTeX code editor. Grammarly was also used to improve the language and provide additional vocabulary corrections in sentences as a final check. All in all, these AI models are not used to generate an output for the thesis project or to incorporate any copied information or data when writing the thesis.